# LJMU Research Online

Turner, DJ, Giles, PA, Romer, AK, Wilkinson, R, Upsdell, EW, Klein, M, Viana, PTP, Hilton, M, Bhargava, S, Collins, CA, Mann, RG, Sahlén, M and Stott, JP

 The XMM Cluster Survey: An independent demonstration of the fidelity of the eFEDS galaxy cluster data products and implications for future studies

http://researchonline.ljmu.ac.uk/id/eprint/19930/

**Article**

For more information please contact researchonline@ljmu.ac.uk

# The *XMM* Cluster Survey: an independent demonstration of the fidelity of the eFEDS galaxy cluster data products and implications for future studies

D. J. Turner [1],[★] P. A. Giles [1],[★] A. K. Romer,[1][★] R. Wilkinson [1], E. W. Upsdell [1], M. Klein,[2] P. T. P. Viana [3,4] M. Hilton [5,6] S. Bhargava,[7] C. A. Collins,[8] R. G. Mann,[9] M. Sahlén [10] and J. P. Stott [11]

[1]*Department of Physics and Astronomy, University of Sussex, Brighton BN1 9QH, UK*
[2]*Faculty of Physics, Ludwig-Maximilians-Universität, Scheinerstr. 1, D-81679 Munich, Germany*
[3]*Instituto de Astrofísica e Ciências do Espaço, Universidade do Porto, CAUP, Rua das Estrelas, P-4150-762 Porto, Portugal*
[4]*Faculdade de Ciências, Departamento de Física e Astronomia, Universidade do Porto, Rua do Campo Alegre, 687, P-4169-007 Porto, Portugal*
[5]*Astrophysics Research Centre, University of KwaZulu-Natal, Westville Campus, Durban 4041, South Africa*
[6]*School of Mathematics, Statistics, and Computer Science, University of KwaZulu-Natal, Westville Campus, Durban 4041, South Africa*
[7]*Département d'Astrophysique, CEA Paris-Saclay, F-91190 Gif-sur-Yvette, France*
[8]*Astrophysics Research Institute, Liverpool John Moores University, Liverpool Science Park, 146 Brownlow Hill, Liverpool L3 5RF, UK*
[9]*Institute for Astronomy, University of Edinburgh, Royal Observatory, Blackford Hill, Edinburgh EH9 3HJ, UK*
[10]*Theoretical Astrophysics, Department of Physics and Astronomy, Uppsala University, Box 516, SE-75120 Uppsala, Sweden*
[11]*Department of Physics, Lancaster University, Lancaster LA1 4YB, UK*

## ABSTRACT

We present the first comparison between properties of clusters of galaxies detected by the eROSITA Final Equatorial-Depth Survey (eFEDS) and the *XMM* Cluster Survey (XCS). We have compared, in an ensemble fashion, properties from the eFEDS X-ray cluster catalogue with those from the Ultimate **X**MM e**X**traga**L**actic (XXL) survey project (XXL-100-GC). We find the redshift and temperature ($T_X$) distributions to be similar, with a larger proportion of clusters above 4 keV in the XXL-100-GC sample; fractional temperature uncertainties are significantly larger in eFEDS compared to XXL. We find 62 eFEDS cluster candidates with *XMM* data (eFEDS-*XMM* sample); 10 do not have good enough *XMM* data to confirm or deny, 11 are classed as sample contaminants, and 4 have their X-ray flux contaminated by another source. The majority of eFEDS-*XMM* sources have longer *XMM* exposures than eFEDS, and most eFEDS positions are within 100 kpc of XCS positions. Our eFEDS-XCS sample of 37 clusters is used to calculate minimum sample contamination fractions of ∼18 and ∼9 per cent in the eFEDS X-ray and optically confirmed samples, respectively, in general agreement with eFEDS findings. We directly compare 29 X-ray luminosities ($L_X$) measured by eFEDS and XCS, finding excellent agreement. Eight clusters have a $T_X$ measured by XCS and eFEDS, and we find that *XMM* temperatures are 25 ± 9 per cent larger than their *eROSITA* counterparts. Finally, we construct $L_X$–$T_X$ scaling relations based on eFEDS and XCS measurements, which are in tension; the tension is decreased when we measure a third scaling relation with calibrated XCS temperatures.

**Key words:** instrumentation: miscellaneous – techniques: spectroscopic – galaxies: clusters: intracluster medium – X-rays: galaxies: clusters.

## 1 INTRODUCTION

X-ray observations of clusters of galaxies provide insights into various aspects of astrophysics (e.g. Hitomi Collaboration et al. 2016; Bhargava et al. 2020; Sanders et al. 2022) and cosmology (e.g. Vikhlinin et al. 2009; Schellenberger & Reiprich 2017). Clusters are among the largest gravitationally bound structures in the Universe and consist of a dark matter halo, the intra-cluster medium (ICM), and the component galaxies. The ICM is a high-temperature, low-density plasma that emits strongly in the X-ray band, with both continuum and emission-line components.

The *eROSITA* instrument mounted on the joint Russian–German Spectrum–Roentgen–Gamma (SRG; Predehl et al. 2021) mission will contribute significantly to X-ray cluster astrophysics and cosmology. Its large field of view (∼1°), sensitivity, and energy resolution combine to make it a revolutionary new instrument. The final *eROSITA* All-Sky Survey (eRASS) is predicted to detect approximately 100 000 galaxy clusters above a mass of $5 \times 10^{13} h^{-1} M_\odot$ (Pillepich, Porciani & Reiprich 2012). The data sharing agreement between the German and Russian consortiums that funded *eROSITA* involves sharing the sky equally. Most of these clusters will be accompanied by an X-ray luminosity ($L_X$) measurement, and roughly 20 per cent (Liu et al. 2021a) of the observations will yield an X-ray temperature ($T_X$) measurement. However, apart from a handful of the highest flux clusters, it will not be possible to measure masses via the hydrostatic technique directly from eRASS data. Therefore, until

* E-mail: david.turner@sussex.ac.uk (DJT); P.A.Giles@sussex.ac.uk (PAG); romer@sussex.ac.uk (AKR)

the all-sky survey is complete, it will be necessary to supplement the eRASS cluster catalogue with mass measurements from the current generation of X-ray telescopes (i.e. *XMM*, *Chandra*) in order to maximize the scientific yield. After the all-sky survey is complete, *eROSITA* pointed observations of clusters, will produce some hydrostatic mass estimates, as demonstrated Sanders et al. (2021).

The aim of this paper is to explore potential synergies between eRASS cluster catalogues and the data in the *XMM–Newton* public archive, and to probe calibration considerations required for such analyses. The *eROSITA* and *XMM* telescopes have different characteristics that allow them to complement one another, some of which (such as the effective area at different energies, and the background level) were explored by Predehl et al. (2021). Comparisons between the on-axis effective areas of the combined *XMM* cameras (PN, MOS1, and MOS2) and the combined *eROSITA* telescope modules show that the effective areas are effectively equal between ∼0.5 and 2.0 keV, though outside this range *XMM* has an advantage. Here *XMM* complements *eROSITA* in that it will observe more source emission at higher energies, which could improve constraints on spectroscopic X-ray measurements of temperature and luminosity. The larger field of view of *eROSITA* ensures that its grasp (the product of effective area and observing area) is significantly greater than *XMM*'s below ∼3.5 keV, though above that energy *XMM*'s grasp is greater. Comparisons between the background levels of a subset of *eROSITA*'s telescope modules and the *XMM–Newton* cameras using a simultaneous observation of NLS1 1H0707−495 (Boller et al. 2021) revealed that, although the *eROSITA* background is higher than pre-launch predictions, it is generally lower than *XMM* and more temporally stable. Soft-proton flaring does not significantly impact *eROSITA*, giving it an advantage over *XMM* in this regard, and possibly allowing it to locate more low-flux sources (such as low-surface-brightness galaxy clusters).

In this work, we will make use of the recent release of the *eROSITA* Final Equatorial-Depth Survey (eFEDS; Brunner et al. 2021). The eFEDS field covers approximately 140 deg² of the equatorial (−2°.5 < δ < 6°.0) sky. It intersects with several optical/near-IR photometric and/or spectroscopic surveys, including the Hyper Suprime-Cam Subaru Strategic Program (HSC SSP; Aihara et al. 2018), the Galaxy and Mass Assembly survey (GAMA; Driver et al. 2011), and the Sloan Digital Sky Survey (SDSS; Blanton et al. 2017). We make an indirect comparison to a similar X-ray survey using the XXL-100-GC catalogue (Pacaud et al. 2016), then make direct comparisons to XCS measurements.

We wish to ascertain the level of sample contamination in the eFEDS cluster catalogue, compare the central coordinates of the detected clusters to those measured by the *XMM* Cluster Survey (XCS; Romer et al. 1999), and verify the accuracy of $L_X$ and $T_X$ measurements. As eFEDS is the same depth as the final eRASS, the accuracy of these measurements have implications for cosmological studies based on eRASS cluster detection (using weak lensing masses and X-ray luminosities for the mass observable relation). They will also impact studies based on optical or near-infrared detection (as luminosities can be used to explore scatter in the mass observable relations), and astrophysical studies of cluster luminosity–temperature relations to study the evolution of the ICM.

There is a known difference between the galaxy cluster temperatures measured by *XMM* and *Chandra*. This difference has been quantified with functions to calibrate the temperatures of one telescope to another; Schellenberger et al. (2015) showed that the difference increases with temperature, with *XMM* EPIC temperatures being on average 7 and 23 per cent lower than *Chandra* ACIS temper-

atures for 2- and 10-keV clusters, respectively. Possible mechanisms for the discrepancy include instrument specific calibration errors (i.e. uncertainty on calculated effective areas), or fitting single-temperature plasma models to multitemperature plasma emission. Schellenberger et al. (2015) demonstrated that multiphase ICM with extreme temperature differences can cause an overall temperature to be dependent on the instrument response. However, they concluded that effective area calibration uncertainties in the soft energy band (0.7-2) keV caused the observed differences in temperature between *XMM* and *Chandra*. Any analysis that uses both *XMM* and *Chandra* temperatures typically accounts for this (e.g. Farahi et al. 2019; Migkas et al. 2020). An understanding of whether there is a similar difference in *eROSITA* and *XMM* temperatures will be necessary before any joint analyses with data from the two telescopes are undertaken, and before scaling relations from one telescope can be safely used by another.

In Section 2, we explore the general properties of the eFEDS cluster catalogue and provide comparisons to a catalogue with similar properties. In Section 3, we construct a cluster sample from the eFEDS catalogue with corresponding *XMM* observations, which includes a visual inspection of the X-ray data and SDSS/HSC images. We also compare eFEDS and XCS exposure times and central positions. In Section 4, we compare luminosities and temperatures measured by eFEDS and XCS. Finally, in Section 5, we generate luminosity–temperature relations, discuss implications of our findings and how they can be improved. Then, in Section 6, we provide a final summary. The analysis code and samples are available in a GitHub repository.[1]

Throughout this work we use a concordance ΛCDM cosmology where $\Omega_M = 0.3$, $\Omega_\Lambda = 0.7$, and $H_0 = 70$ km s⁻¹ Mpc⁻¹, consistent with the original eFEDS cluster analysis (and other XCS works).

## 2 COMPARISON OF THE EFEDS OPTICALLY CONFIRMED AND XXL-100-GC CATALOGUES

The eFEDS cluster catalogue (Liu et al. 2021a) contains 542 candidates, 477 of which are considered to be optically confirmed (Klein et al. 2022) when assessed using the Multi-component Matched Filter Cluster Confirmation Tool (MCMF; Klein et al. 2018). All 542 X-ray candidates are accompanied by redshift ($z$) values. Soft-band (0.5-2.0 keV in the source frame) $L_X$ values have been measured for 91 per cent of the X-ray cluster candidate sample. A smaller percentage, 21 per cent, of $T_X$ values were obtained using spectra extracted from circular apertures centred on the eFEDS coordinates; 69 within 300 kpc, and 95 within 500 kpc (102 candidates have at least one temperature measurement).

The XXL survey (Pierre et al. 2016) covers ∼50 deg² of the sky (over two separate regions), making it the largest contiguous area survey in the *XMM* archive. It consists of 542 separate *XMM* observations with on-axis exposure times ranging from 10 to 20 ks. The contiguous nature of XXL makes it ideal to compare to eFEDS. As eFEDS and the XXL survey were taken in different parts of the sky there are no clusters in common. Although we note that the X-CLASS analysis of the *XMM* archive (up to 2015 August) that made use of the XXL pipelines does contain some eFEDS candidates (Koulouridis et al. 2021). Comparisons are limited to ensemble distributions of the cluster samples. We made use of the XXL-100-GC sample (Pacaud et al. 2016), containing the 100 brightest galaxy clusters observed in XXL, and the sample of 477 optically confirmed eFEDS candidates.

---

[1]Analysis code and samples
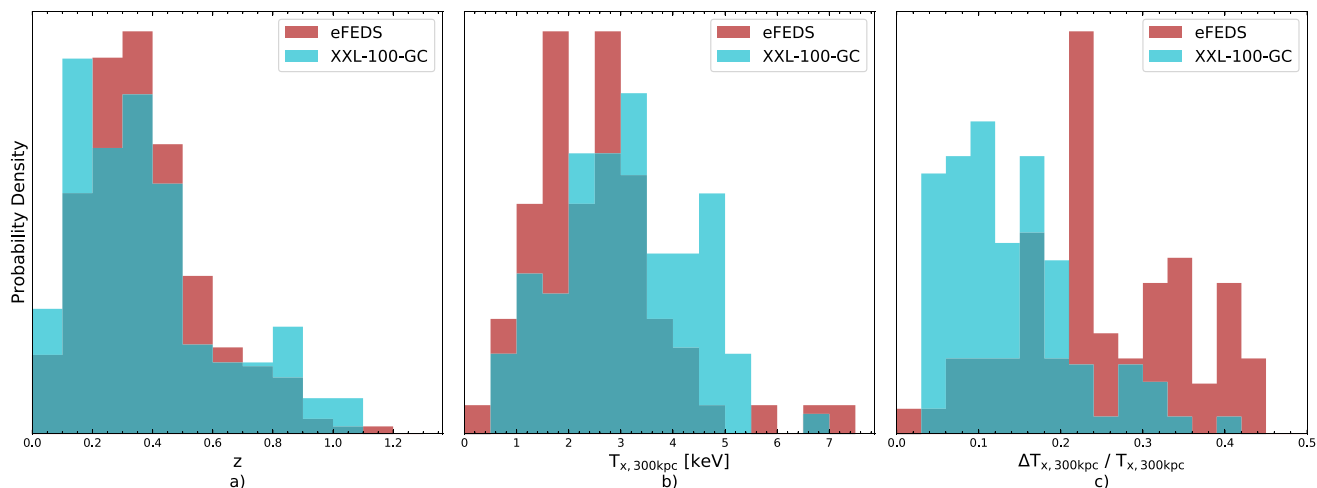
**Figure 1.** Redshift, temperature, and fractional temperature error distributions of the eFEDS and XXL-100-GC samples. Redshifts from both samples come from a variety of sources, and temperatures are measured within 300-kpc apertures centred on clusters. There are no clusters in common between the two samples.

The flux limits of the eFEDS and XXL-100-GC cluster samples are similar; $\sim 10^{-14}$ erg s$^{-1}$ cm$^{-2}$.

Fig. 1(a) shows the redshift distributions of the clusters in the two samples (eFEDS and XXL-100-GC distributions are shown in red and cyan respectively) to be very similar overall, but that XXL-100-GC detects a higher proportion of clusters at low redshifts. Next, we compare the respective temperature distributions. Temperatures for the XXL-100-GC clusters were measured within a 300-kpc aperture (Giles et al. 2016), as were temperatures for eFEDS clusters, making a direct comparison of the distributions valid. Fig. 1(b) plots the temperature distributions of the two samples, with the XXL-100-GC temperature distribution containing a significantly higher proportion of temperatures above $\sim 3.5$ keV. Liu et al. (2021a) note that *eROSITA*'s ability to measure temperatures for hot clusters at $\gtrsim 5$ keV is limited due to the reduced sensitivity of *eROSITA* at energies $>3$ keV. This is a plausible reason for the increased number of higher temperature clusters in XXL-100-GC compared to eFEDS. The effective area of *eROSITA* is $\sim 150$ cm$^2$ at 5 keV, compared to $\sim 900$ cm$^2$ for EPIC-PN; see fig. 9 in Predehl et al. (2021) for a detailed comparison. Previous work by Lloyd-Davies et al. (2011) has also shown that more counts are required to constrain temperatures to the same level for hotter galaxy clusters. Furthermore, the temperature distribution could also be influenced by the selection functions of the two surveys, differing measurement methodology, or a systematic difference in temperatures measured by the *eROSITA* and *XMM* telescopes (we explore this in Section 4.4).

Finally, we compare how well temperatures from the two samples are constrained, by comparing temperature uncertainties as a fraction of the absolute temperature value ($\Delta T_X/T_X$). Fig. 1(c) shows that, on average, XXL achieves better temperature constraints than eFEDS, with the mean percentage uncertainties for XXL and eFEDS being 14 and 25 per cent respectively. This is consistent with the findings of Lloyd-Davies et al. (2011), who showed that $\sim 1000$ background-subtracted soft-band (0.5–2.0 keV) counts are required to achieve a fractional temperature uncertainty of $\sim 0.1$ for a 3-keV cluster. In this regard the longer exposures of XXL compared to eFEDS would give an advantage (especially in the deeper *XMM*-LSS fields, covering $\sim 11$ deg$^2$ in the XXL-N field).

## 3 UNDERSTANDING THE EFEDS CATALOGUE CONTAMINATION FRACTION

In this section, we make use of archival *XMM* data that overlaps with the eFEDS footprint to assemble samples for analysis, and make an estimate of the contamination fraction in the eFEDS cluster candidate list. For this, we have used data products (images and source lists) generated by the XCS (Romer et al. 1999). The XCS source lists are constructed by the XCS Automated Pipeline Algorithm (XAPA) source finder, and a full explanation of our procedures can be found in Lloyd-Davies et al. (2011). We first determine which eFEDS X-ray cluster candidates fall within the active area of an *XMM* observation (Section 3.1). For these, we generate *eROSITA* cut-out images. We then compare, by eye, to the corresponding *XMM* cut-outs (Section 3.2). We also compare to optical SDSS DR16 (Ahumada et al. 2020) images obtained from the SDSS cutout server.[2] As $\sim 70$ per cent of the eFEDS-XMM sample are at redshifts $z < 0.5$ it is generally appropriate to search for a red sequence using SDSS imagery, however for any candidate that we could not confirm with SDSS, we then examined images taken from the second data release of the HSC-SSP (PDR2; Aihara et al. 2019).[3] The deeper data of HSC-SSP PDR2 (*i*-band limiting magnitude of 26.2 in the wide field, where the SDSS DR16 *i*-band limiting magnitude is 22.2) allow for detection of cluster galaxies at much higher redshifts. Our visual inspection allows us to categorize contaminating objects (Section 3.3) and to estimate the overall contamination fraction in the eFEDS sample (Section 3.5).

### 3.1 eFEDS cluster candidates in the *XMM* footprint

Fig. 2 shows the outline of the eFEDS footprint with eFEDS X-ray cluster candidates (Liu et al. 2021a) indicated by red diamonds. *XMM* observations taken within the eFEDS footprint are indicated by grey shaded circles, with a radius of 15 arcmin (the approximate radius of the *XMM* field of view). There are a total of 143 *XMM*

---

[2]SDSS Image Cutout Server.
[3]HSC-SSP PDR2 Image Cutout Server.
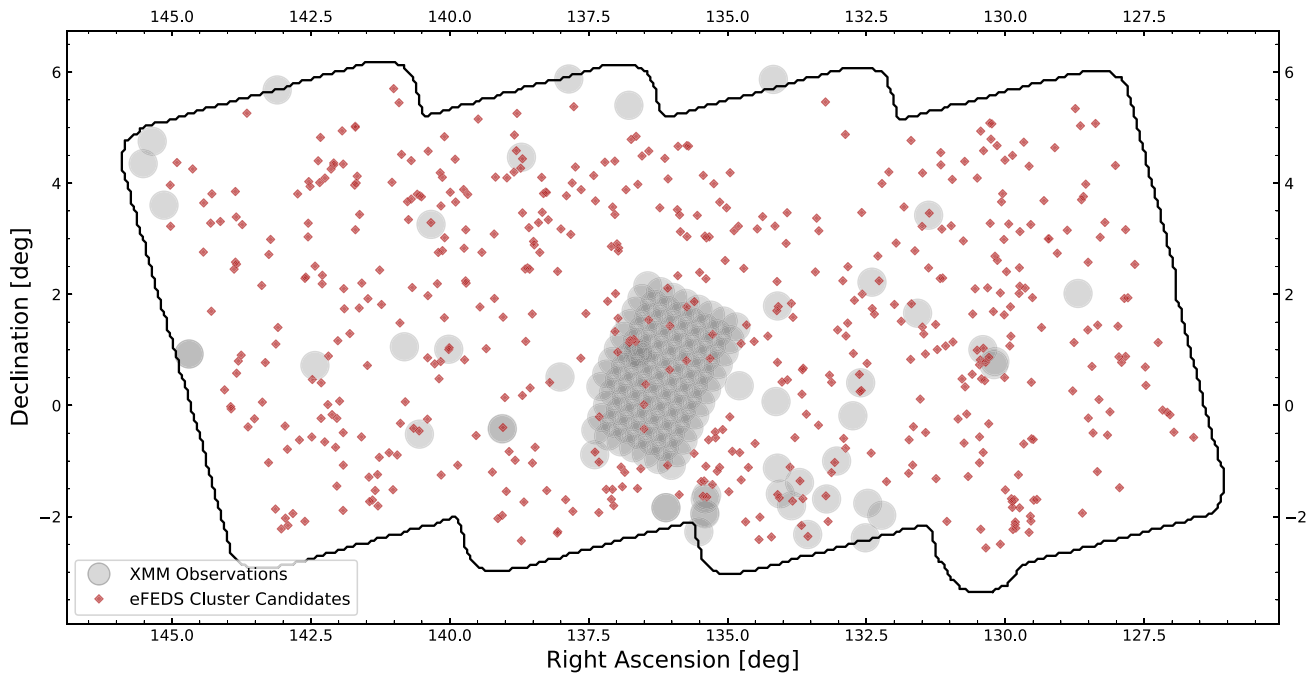
**Figure 2.** Footprint of eFEDS, given by the black solid line. Cluster candidates present in the eFEDS X-ray catalogue are highlighted by red diamonds. The grey circles highlight *XMM* observations, with a radius of 15 arcmin (the approximate radius of the *XMM* FoV).

**Table 1.** Summary of the samples defined in this work.

| Sample name | Description | $N_{cl}$ | $NT_{eFEDS, 500\,kpc}$ | $NT_{XCS, 500\,kpc}$ |
|---|---|---|---|---|
| eFEDS | The full eFEDS cluster candidates catalogue | 542 | 95 | – |
| eFEDS-*XMM* | eFEDS cluster candidates that fall on an *XMM* observation | 62 | 11 | – |
| eFEDS-XCS | eFEDS-*XMM* candidates available for analysis after inspection | 37 | 8 | 28 |

*Note.* $N_{cl}$ is the number of clusters, $NT_{eFEDS,\,500\,kpc}$ is the number with eFEDS $T_{500\,kpc}$ values, and $NT_{XCS,\,500\,kpc}$ is the number with XCS $T_{500\,kpc}$ values.

observations, covering ∼15 deg² (11 per cent) of the sky within the eFEDS footprint, accounting for overlapping *XMM* observations.

We used X-ray: Generate and Analyse (xGA[4]; Turner et al. 2022); a new, open-source, X-ray astronomy analysis module developed by XCS, to determine which of the 542 eFEDS cluster candidates listed in Liu et al. (2021a) have also been observed by *XMM*. An initial search finds eFEDS candidates with central coordinates within 30 arcmin of an *XMM* observation aim-point (this is larger than the *XMM* field of view to account for any cases of low-$z$ clusters with centroid offsets). We then refined the match so that at least 70 per cent of a 300 kpc aperture (centred on the eFEDS coordinate and assuming the eFEDS redshift) coincides with an *XMM* observation. In sum, 62 eFEDS candidates met these criteria, and this subset is denoted the eFEDS-*XMM* sample (see Table 1). Fifty-three of the eFEDS-*XMM* candidates appear in the eFEDS optically confirmed sample (Klein et al. 2022).

The distribution of *XMM* exposure times for the eFEDS-*XMM* sample is shown in Fig. 3. The light-blue distribution uses the best individual observation exposure time for each eFEDS-*XMM* candidate; the grey distribution is the total exposure time for each candidate. These are vignetting-corrected exposure times at the

eFEDS coordinate (rather than at the respective observation aim-point). The typical eFEDS vignetting-corrected exposure (1.2 ks) is shown by the dashed red line for comparison. The majority of exposure times (individual or total) are longer for *XMM* than eFEDS.

### 3.2 Constructing the eFEDS-XCS sample

To judge the quality of the eFEDS candidates in the eFEDS-*XMM* sample, circular cut-out images, of radius 500 kpc, were generated from the *eROSITA* eFEDS data and XCS-processed *XMM* data. We select the *XMM* observation with the highest signal-to-noise within a 300-kpc aperture centred on the eFEDS candidate coordinate, and use its XCS-generated PN + MOS1 + MOS2 image (Giles et al. 2022). For the *eROSITA* cut-outs, the eSASS[5] (Brunner et al. 2018) EVTOOL software was used.

Both sets of images used a pixel size of 4.35 arcsec, but different energy ranges were used; 0.5–2.0 keV for *XMM* and 0.2–2.3 keV for *eROSITA*. These ranges reflect those used by the respective XCS and eFEDS source detection routines.

As shown in Predehl et al. (2021), the energy-dependent effective area of *XMM* (assuming all three cameras are operating) is the same,

---

[4]X-ray: Generate and Analyse GitHub.

[5]Introduction to eSASS.
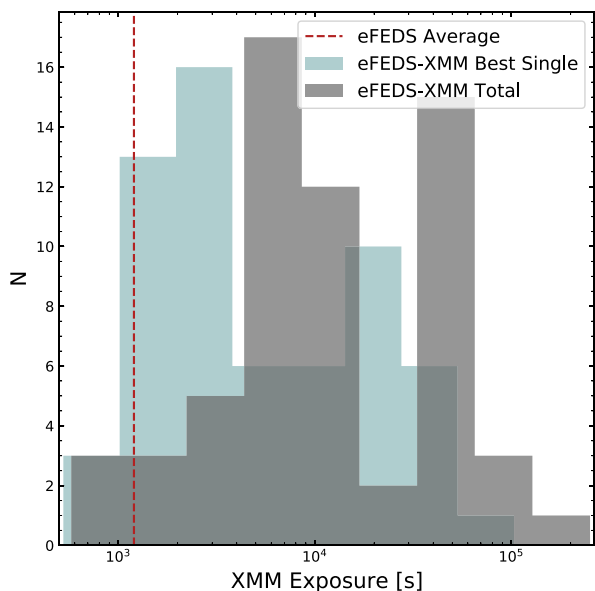
**Figure 3.** Distribution of exposure times for eFEDS-*XMM* cluster candidates, measured at the eFEDS coordinates. Exposures taken from 0.5–2.0 keV exposure maps, corrected for flaring and vignetting. Dashed line indicates the average vignetting corrected exposure of the eFEDS field reported by Liu et al. (2021a).



**Figure 4.** Comparison of eFEDS and XAPA central coordinates, for the subset of the eFEDS-XCS sample that have been detected by XAPA.

or greater, than that of *eROSITA*. Therefore, we can expect most of the *XMM* cut-outs to have higher signal-to-noise ratio than their eFEDS counterparts, even after accounting for the fact that the *XMM* background level is slightly higher than *eROSITA*'s. In 10 cases, however, we judged the *XMM* data to be inadequate for further analysis. This was either because the eFEDS candidate fell on the edge of the field of view and/or because the signal-to-noise ratio was too low (see Table A1 for details). These 10 were excluded from further analysis, although it is noteworthy that in 5 cases, an obvious (by eye) extended source was visible in the corresponding *eROSITA* cut-out.

The remaining 52 eFEDS-*XMM* sources were then visually inspected side by side to judge the quality of the eFEDS candidates. In sum, 37 eFEDS-*XMM* candidates were confirmed as clusters suitable for X-ray analysis by this visual inspection, henceforth called the eFEDS-XCS sample. Generally speaking, the XCS- and eFEDS-defined centroid positions were in good agreement (with an offset of less than 100 kpc), but several outliers are present (see Fig. 4). The outliers were due to either low signal-to-noise eFEDS data, or to eFEDS point source contamination. Similar examples were noted in Klein et al. (2022).

The other eFEDS cluster candidates were classified as sample contaminants (11, Table A2), or as having their X-ray flux contaminated by other sources (4, Table A3). There are three broad categories of sample contamination, as described below (Section 3.3).

### 3.3 Categories of contaminating objects in the eFEDS X-ray cluster candidate catalogue

Here we discuss categories for the different types of contaminating object that we discovered in the eFEDS X-ray cluster candidate catalogue. The figures that we use to illustrate these examples are not necessarily on the same scale, or centred on the same position, as those we used for visual inspection, and all figures use HSC imagery
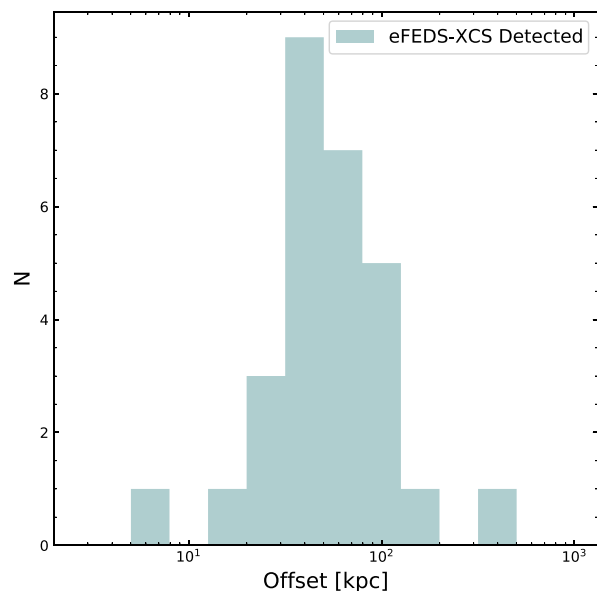
for clarity. The optical images we used for general inspection were SDSS, with HSC photometry used in cases were we needed to clarify our classification.

#### 3.3.1 Blended sources

An example of this is eFEDS ID 1644, which is shown in Fig. 5; the two sources at the centre of the *XMM* image (Fig. 5, left-hand panel; detected as separate point sources by XCS) in the *XMM* cut-out appear as a single object in the *eROSITA* image. The dominant X-ray source is discussed in Pfeifle et al. (2019). It is the result of AGN activity in a pair of interacting galaxies. The two galaxies can be seen in the corresponding HSC image in Fig. 5 (right-hand panel). The blending is likely a result of *eROSITA*'s 26-arcsec FOV average PSF half-energy width (HEW), which is larger than the *XMM* PN camera's 16.5-arcsec PSF HEW (at 1.5 keV), in combination with the short eFEDS exposure time. This source was assigned a class of B2 during the MCMF classification process, which indicates point source contamination, but it is still retained in the optically confirmed catalogue.

#### 3.3.2 Spurious sources

An example of this is shown in Fig. 6. There does not appear to be a source at the eFEDS candidate centroid position (extended or otherwise) in either the *XMM* or *eROSITA* image (Fig. 6, left-hand and middle panels, respectively). We note that the redshift provided by the eFEDS cluster catalogue for this candidate (eFEDS ID 3334) is very low ($z = 0.087$) and so any X-ray cluster emission should be obvious, unless it is very low surface brightness and/or very extended. Nonetheless, we do not see evidence of a coincident population of galaxies in the HSC imagery (Fig. 6, right-hand panel).

Another example is eFEDS ID 8922, which is shown in Fig. 7; this cutout is not centred on the spurious eFEDS cluster candidate, but on the bright source that causes it. The eFEDS candidate location (at the cross-hairs) is in the outskirts of a bright source (eFEDS ID 3, not
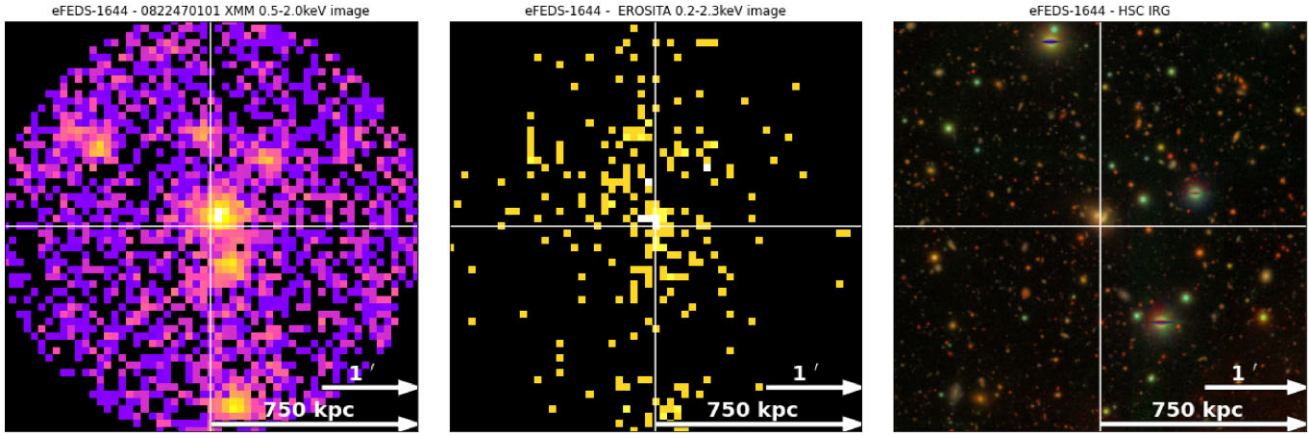
**Figure 5.** eFEDS-*XMM* cluster candidate (eFEDS ID 1644) identified as a pair interacting galaxies with ongoing AGN activity (see Section 3.3.1). The cross-hair 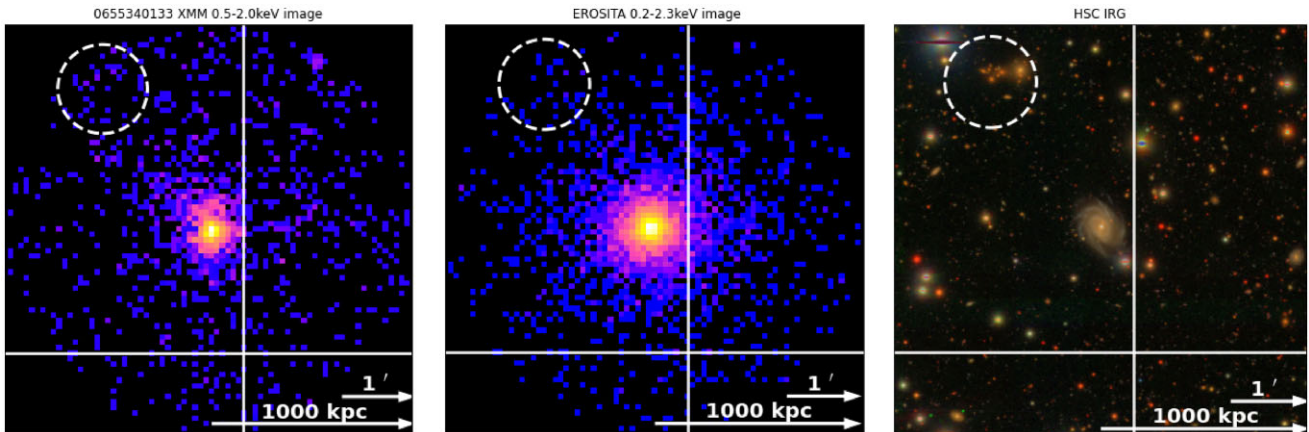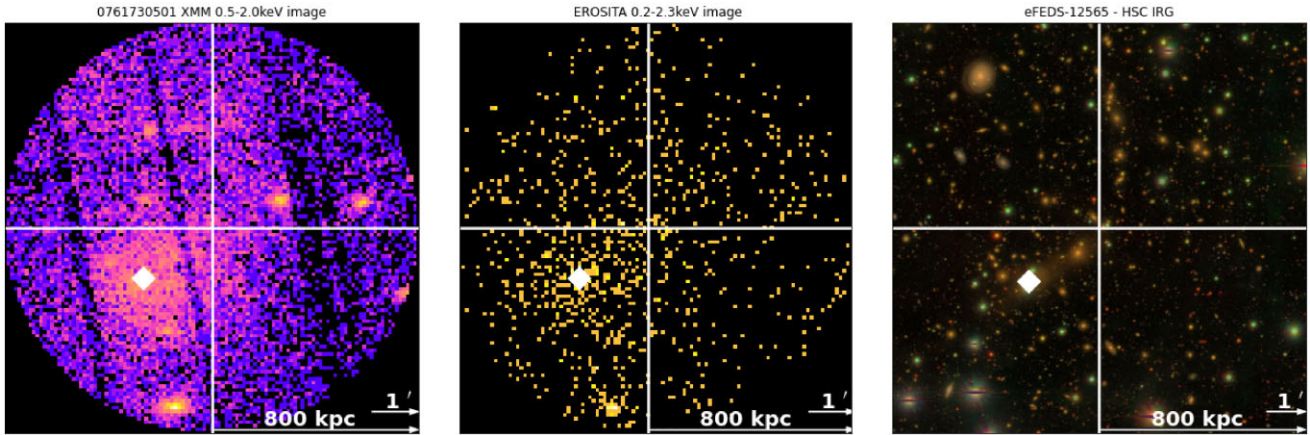indicates the eFEDS position. The left-hand side is a combined PN+MOS1 + MOS2 *XMM* image (ObsID 0822470101), centre is *eROSITA*, and the right-hand side is HSC. Both *XMM* and *eROSITA* images are cutouts within a radius of 750 kpc, and the HSC image has a half-side-length of 750 kpc (at the redshift provided by eFEDS).
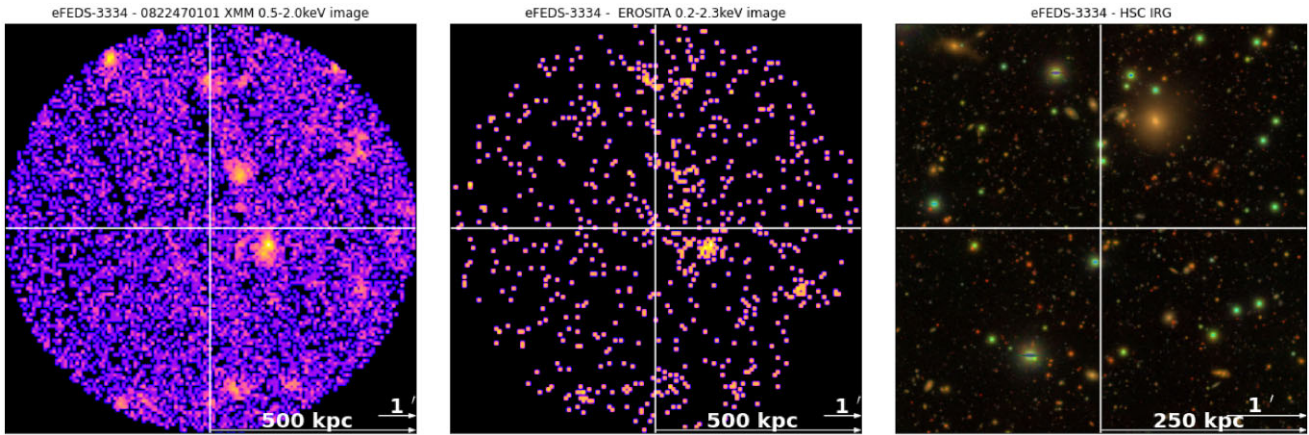


**Figure 6.** eFEDS-*XMM* cluster candidate (eFEDS ID 3334) without an obvious corresponding source of emission (see Section 3.3.2). The cross-hair indicates the eFEDS position. The left-hand side is a combined PN+MOS1 + MOS2 *XMM* image (ObsID 0822470101), centre is *eROSITA*, and the right-hand side is HSC. Both *XMM* and *eROSITA* images are cutouts within a radius of 500 kpc, and the HSC image has a smaller half-side-length of 250 kpc (at the redshift provided by eFEDS).



**Figure 7.** Two eFEDS-*XMM* cluster candidates in the outskirts of a low redshift foreground AGN. A spurious eFEDS-*XMM* cluster candidate (eFEDS ID 8922) is indicated by the cross-hair (see Section 3.3.2). An eFEDS-*XMM* cluster candidate (eFEDS ID 16370) is indicated by the dashed circle. The left-hand side is a combined PN+MOS1 + MOS2 *XMM* image (ObsID 0655340133), centre is *eROSITA*, and the right-hand side is HSC. Both *XMM* and *eROSITA* images are cutouts within a radius of 1000 kpc, and the HSC image has a half-side-length of 1000 kpc (at the redshift for eFEDS ID 8922 provided by eFEDS).

**Figure 8.** eFEDS galaxy cluster split into two candidates by the source finder (see Section 3.3.3). Cross-hairs indicate one candidate (eFEDS ID 8602), and the white diamond indicates the other (eFEDS ID 1023). The left-hand side is a combined PN+MOS1 + MOS2 *XMM* image (ObsID 0761730501), centre is *eROSITA*, and the right-hand side is HSC. Both *XMM* and *eROSITA* images are cutouts within a radius of 800 kpc, and the HSC image has a half-side-length of 800 kpc (at the redshift provided by eFEDS, which is the same for 8602 and 1023).

present in the cluster candidate catalogue), and not coincident with any distinct source in either the *XMM* or *eROSITA* image (Fig. 7, left-hand and middle panels, respectively). There also does not appear to be an association of galaxies in HSC imagery (Fig. 7, right-hand panel). The dominant X-ray source is identified as an AGN in the Million Quasar catalogue (Flesch 2021) located in a spiral galaxy visible in the corresponding optical image. It is also present in the eFEDS AGN catalogue (Liu et al. 2022).

### 3.3.3 Fragmented sources

An example of this is shown in Fig. 8. The white cross-hair indicating the position of one eFEDS candidate (eFEDS ID 8602), and the white diamond another (eFEDS ID 1023). The two candidates have almost identical redshifts ($z = 0.196$ and 0.197, respectively). Luminosity measurements for both, and a temperature estimate for eFEDS ID 1023, are given in Liu et al. (2021a). We discuss this system further in Appendix B. We note that it is not used during our luminosity (Section 4.2) and temperature comparisons (Section 4.3 and Section 4.4), or in our luminosity–temperature relation analysis (Section 5.1).

### 3.4 Clusters with contaminated X-ray emission

In these cases there is evidence, from the SDSS and/or HSC data, for a physical association of galaxies – which could, in turn, be responsible for an extended X-ray source due to emission from a hot ICM – however, we contend that any ICM emission present is significantly contaminated by other X-ray sources. One example (eFEDS ID 150) is shown in Fig. 9, where the emission detected by *eROSITA* appears to originate primarily from the central galaxy (alternative, but less likely explanations are that this is a fossil group or a system with a strong cool core). We note that similar examples were identified in eFEDS, candidates with IDs 3133 and 3008 (see Table A3). An example of a different type of contaminated emission is presented in Fig. 7 (eFEDS ID 16370). The eFEDS candidate is highlighted by the white dashed circle. There is tentative evidence of X-ray emission in the *XMM* observation (especially when smoothing is applied), and the coordinates coincide with a collection of red galaxies in SDSS and HSC at an SDSS photo-$z$ of $z = 0.44$ (matching the

eFEDS catalogue's $z$). However, due to the proximity of the eFEDS candidate to the bright AGN (as discussed in Section 3.3.2), the X-ray flux in this region will be contaminated by non ICM emission, so we exclude this cluster from the following analyses.

In this paper we focus on the comparison of the X-ray properties measured by *eROSITA* and *XMM*, so we do not include these four eFEDS candidates in the analyses presented Section 4. However, it would inappropriate to remove them from some other types of analyses – such as cluster number count cosmology based on optical/near-IR selection Klein et al. (2022) – because they are still associated with galaxy overdensities. All of the sources in Table A3 appear in the eFEDS optically confirmed sample.

### 3.5 The eFEDS contamination fraction

As discussed in Section 3.2 (and collated in Appendix A), 11 of the 62 candidates (18 per cent, Table A2) in the eFEDS-*XMM* sample were not included in the eFEDS-XCS sample because they were classified as being in one of the three sample contaminant types described in Section 3.3. This should be viewed as a lower limit because, in 10 (of 62) cases (Table A1), it was not possible for us to confirm the validity of the eFEDS candidate using archival *XMM* data.

The eFEDS-XCS sample of eFEDS cluster candidates is an order of magnitude smaller than the full eFEDS X-ray cluster candidate catalogue. Moreover, several of the eFEDS-XCS clusters were the target of their respective *XMM* observations, and that has been shown to introduce selection bias (Giles et al. 2022); this could influence *XMM* detections and thus the construction of our eFEDS-XCS sample. Even so, our result is consistent with simulations performed by the eRASS team that predicted a contamination level of ∼20 per cent (Comparat et al. 2020). It is also consistent with the eFEDS optical counterparts study (Klein et al. 2022), which measured a contamination fraction of $17 \pm 3$ per cent.

We also investigated whether any of the 11 cluster candidates that we classed as sample contaminants (Table A2) are present in the sample of 477 candidates that Klein et al. (2022) consider to be optically confirmed. We find that 5 of the 11 are present therein. This compares to 53 in the overall eFEDS-*XMM* sample, indicating a minimum contamination fraction of ∼9 per cent in the Klein et al. (2022) sample. This is slightly high compared to the value of $6 \pm 3$ per cent reported by Klein et al. (2022). However, if
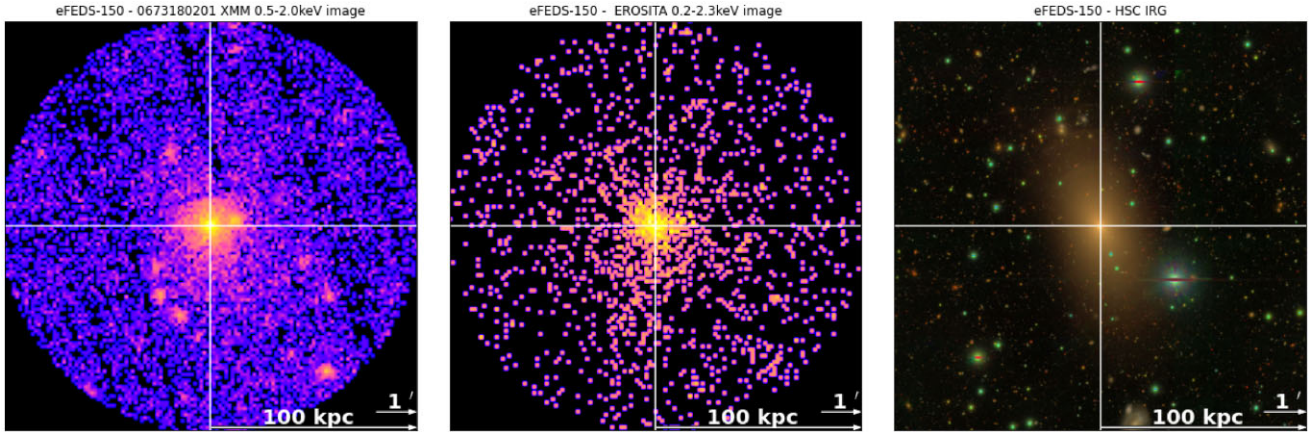
**Figure 9.** A low-redshift eFEDS-*XMM* cluster candidate (eFEDS ID 150) whose X-ray emission is dominated by an X-ray bright elliptical galaxy (see Section 3.4). The left-hand side is a combined PN+MOS1 + MOS2 *XMM* image (ObsID 0673180201), centre is *eROSITA*, and the right-hand side is HSC. Both *XMM* and *eROSITA* images are cutouts within a radius of 100 kpc, and the HSC image has a half-side-length of 100 kpc (at the redshift provided by eFEDS).

we discount eFEDS ID 8602 and 3334 from consideration as sample contaminants (to be more consistent with approach taken in Klein et al. 2022), the contamination level drops to ∼6 per cent.

We note that one cluster of the eFEDS-XCS sample (eFEDS ID 5170) does not appear in the Klein et al. (2022) sample. This candidate was included in our sample because of its X-ray emission (in *XMM* and *eROSITA* images) and evidence of an overdensity of red galaxies in the SDSS and HSC photometry.

## 4 COMPARISONS OF CLUSTER PROPERTIES MEASURED BY EFEDS AND XCS

We use the XGA (Turner et al. 2022), SAS (Gabriel et al. 2004) and XSPEC (Arnaud 1996) interfaces to generate spectra and fit models to them, for those clusters that have high enough quality *XMM* data. We then compare values to those presented in the eFEDS data release. Note that we do not re-analyse the eFEDS data, but compare to the measurements given by Liu et al. (2021a). We use XGA v0.2.1, SAS v17.0.0, and XSPEC v12.10.1.

### 4.1 Fitting procedure

Cluster spectra are extracted within a 500-kpc fixed aperture (as the eFEDS catalogue contains a greater number of 500-kpc temperatures than 300 kpc) and centred on the eFEDS position. Corresponding backgrounds are extracted within 1000–1500 kpc annuli. Non-cluster sources in both the 500-kpc apertures and background regions are identified using the XCS region files, and their corresponding events are removed during spectrum generation. The SAS evselect tool is used to generate spectra from all available *XMM* data for an eFEDS-XCS cluster (EPIC-PN, EPIC-MOS1, and EPIC-MOS2 cameras are all used; see Table C1 for the data used for each cluster). Spectra are re-binned using the SAS specgroup so that there are a minimum of five counts per channel. Ancillary files are calculated using rmfgen and arfgen, with an image in detector coordinates used as a detector map for ARF generation.

We fit absorbed (with tbabs; Wilms, Allen & McCray 2000) plasma emission models (APEC; Smith et al. 2001) to the spectra; these models are standard for XCS analyses, but are also the same as those used in the eFEDS spectroscopic analysis. To maximize the similarity of our analysis to eFEDS, we opt to use the abundance tables published by Asplund et al. (2009) when performing our

spectral fits. The abundance parameter of the APEC model in all cases is frozen at 0.3 $Z_\odot$, the $n_H$ parameter of the tbabs model is set from the full-sky H I survey by the HI4PI Collaboration et al. (2016) using the HEASOFT nh tool and frozen. The redshift parameter is set to the eFEDS catalogue value and frozen. The temperature is initially set to 3 keV and the normalization is initially set to 1 cm$^{-5}$, then both are allowed to vary.

Each individual spectrum (each instrument for each *XMM* observation) is first fit independently, and if the measured temperature is outside of the range $0.01 \leq T_X < 20$ keV, or either temperature uncertainty is $> 15$ keV, then the spectrum will not be included in the final fit. A simultaneous fit is then performed using only the spectra that fulfil the requirements outlined above. A multiplicative constant is added to the model for the simultaneous fit, and is allowed to vary independently for each spectrum in the fit to account for different instrumental responses, whereas every other model parameter is tied together. Temperatures and unabsorbed luminosities are then determined from this joint fit. We used a given temperature measurement in further analyses (Sections 4.3, 4.4, and 5.1) if (a) the best fit value is less than 25 keV, (b) the upper and lower uncertainties are both positive, and (c) the larger uncertainty is less than three times the smaller. Likewise, fitted luminosities are used in our analyses (Sections 4.2 and 5.1), if both the upper and lower uncertainties are not greater than the best-fitting value, and if the upper and lower uncertainties are both positive.

For a more complete explanation of the spectral fitting process and comparisons of results with other *XMM* analyses that confirm the veracity of measurements produced by this procedure, see Turner et al. (in preparation). All *XMM* measurements for the eFEDS-XCS sample can be found in Table C2, along with the eFEDS ID, position, and redshift.

### 4.2 Luminosity comparison

We compare luminosities measured with both *XMM* and *eROSITA*, since one of the main products of eRASS will be large catalogues of X-ray cluster luminosities. These will be used as the basis of various *eROSITA* science applications; for example, a mass–luminosity scaling relation (such as the one recently produced by Chiu et al. 2021) provides a way to estimate masses and overdensity radii of a given cluster, enabling X-ray cluster cosmology. Therefore,
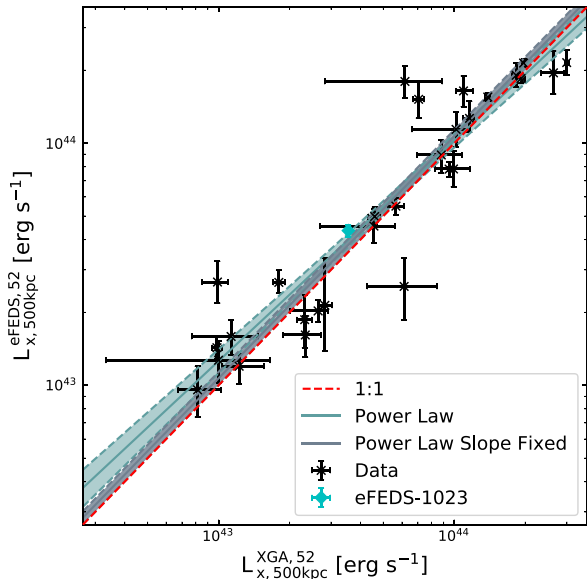
**Figure 10.** Comparison of unabsorbed cluster luminosities within a 500-kpc aperture, in the 0.5–2.0 keV energy band, centred on eFEDS coordinates. The pale blue line indicates the best fit power-law, with 68 per cent confidence levels given by the shaded region. The grey line indicates a power-law fit with the slope set to 1 (with 68 per cent confidence levels given by grey shaded region). The cyan diamond is for the split cluster discussed in Appendix B.

it is important to test the fidelity of eFEDS luminosities with *XMM* data.

The eFEDS analysis presents cluster luminosities measured via a forward-fitting analysis of 2D count-rate maps, including considerations of the morphology of the cluster, rather than by the fitting of emission models to spectroscopic data. In the context of eFEDS, this allows for the measurement of accurate luminosities for clusters that do not have high enough quality data to perform spectral fitting. We can directly compare *XMM* and *eROSITA* luminosities for 29 (∼80 per cent) of the eFEDS-XCS sample. We use a spectral fitting process to measure unabsorbed (corrected for hydrogen column absorption) luminosities in the soft (0.5-2.0keV) energy band for those clusters with a successful *XMM* temperature measurement.

We fit a power law with the slope fixed at unity and another power law with the slope left to vary to the luminosity comparison, finding the results of both to be entirely consistent with a one-to-one relation. The fits were performed in log space using the R package LInear Regression in Astronomy (LIRA[6]; Sereno 2016a), fully described in Sereno (2016b). Fig. 10 demonstrates an excellent soft-band luminosity agreement (including the two models) between eFEDS and XCS, especially considering the differing measurement methods. We also include the data point for the cluster eFEDS ID 1023 (discussed further in Appendix B), but do not include it in our comparison fit. Luminosities measured by eFEDS and XCS are similarly well constrained, though the XCS uncertainties tend to be slightly smaller.

### 4.3 Temperature comparison

We have been able to measure *XMM* temperatures within a 500-kpc aperture for ∼80 per cent (28) of the eFEDS-XCS sample,

[6]LInear Regression in Astronomy.

though only ∼30 per cent (8) of those also have an eFEDS *eROSITA* temperature available (see Table 1 for a summary). We first compare the overall temperature, and fractional temperature uncertainty, distributions, as we did in Section 2 with the XXL-100-GC sample.

Fig. 11(a), which shows the overall distributions of the eFEDS *eROSITA* temperature and eFEDS-XCS *XMM* temperature samples, demonstrates that a larger proportion of *XMM* temperatures than *eROSITA* temperatures are above ∼4 keV, similar to the behaviour in Fig. 1(b) with the XXL-100-GC sample. It is likely that this is due to the difference in telescope sensitivity at high energies, as well as other selection effects resulting from targeted *XMM* exposures.

Fig. 11(b) demonstrates that a larger proportion of the *XMM* temperatures from the eFEDS-XCS sample (compared to *eROSITA* measurements of the eFEDS sample) have a fractional temperature uncertainty of less than 20 per cent, and as such the *XMM* temperature measurements are generally better constrained. However we also note that the temperature fractional error distribution of the eFEDS-XCS sample extends to larger values than eFEDS.

In summary, archival *XMM* observations can provide temperatures that are, on average, better constrained than eFEDS for those clusters that have been observed by *XMM*, and can also deliver more temperatures for hotter systems due to *XMM*'s greater sensitivity at high energies. As such, the *XMM* archive will be a very useful complement to the eRASS.

### 4.4 Temperature calibration

Motivated by the known temperature offset between *XMM* and *Chandra* (Schellenberger et al. 2015), we test for a difference in temperatures measured by *XMM* and *eROSITA*. We use eight *XMM* temperatures that we have measured for a subset of the eFEDS-XCS cluster sample that have *eROSITA* temperatures presented in the eFEDS cluster catalogue to perform a comparison.

The comparison of eight clusters with measured *XMM* and *eROSITA* (eFEDS) temperatures is given in Fig. 12, and shows a systematic offset between the two telescopes. We also plot the data point for the cluster with eFEDS ID 1023 (discussed further in Appendix B), but do not include it in our comparison fit. All but one of the clusters are below the one-to-one line, indicating that the *eROSITA* temperatures are systematically lower than their *XMM* counterparts. To model this, we fit a power law of the form:

$$\log\left(T_{x,500\,kpc}^{eROSITA}\right) = \log(A_{TT}) + B_{TT}\log\left(T_{x,500\,kpc}^{XMM}\right)$$
$$\pm\, \sigma_{T_{eROSITA}|T_{XMM}}, \qquad (1)$$

where $A_{TT}$ is the normalization, $B_{TT}$ is the slope, and $\sigma_{T_{eROSITA}|T_{XMM}}$ is the intrinsic scatter. The fits were performed in the same way as those in Section 4.2. The best-fitting parameters are given in Table 2.

First, we fit the power law with the slope left free to vary, probing whether the observed offset evolves with temperature (as found in Schellenberger et al. 2015, comparing between *Chandra* and *XMM*). We measure a slope value of $0.89^{+0.25}_{-0.24}$, indicating that the calibration evolves with system temperature. We note however that due to the large errors, the value of $B_{TT}$ is consistent with 1 (within $1\sigma$). The measured intrinsic scatter of both fits is very low (essentially consistent with zero), which is as expected. Due to the large errors on the measured slope, we re-fit the power law with the slope fixed at unity. This allows us to measure a single overall normalization that describes the average difference in temperatures measured by the two telescopes. We measure a normalization of $0.75^{+0.10}_{-0.08}$, meaning that
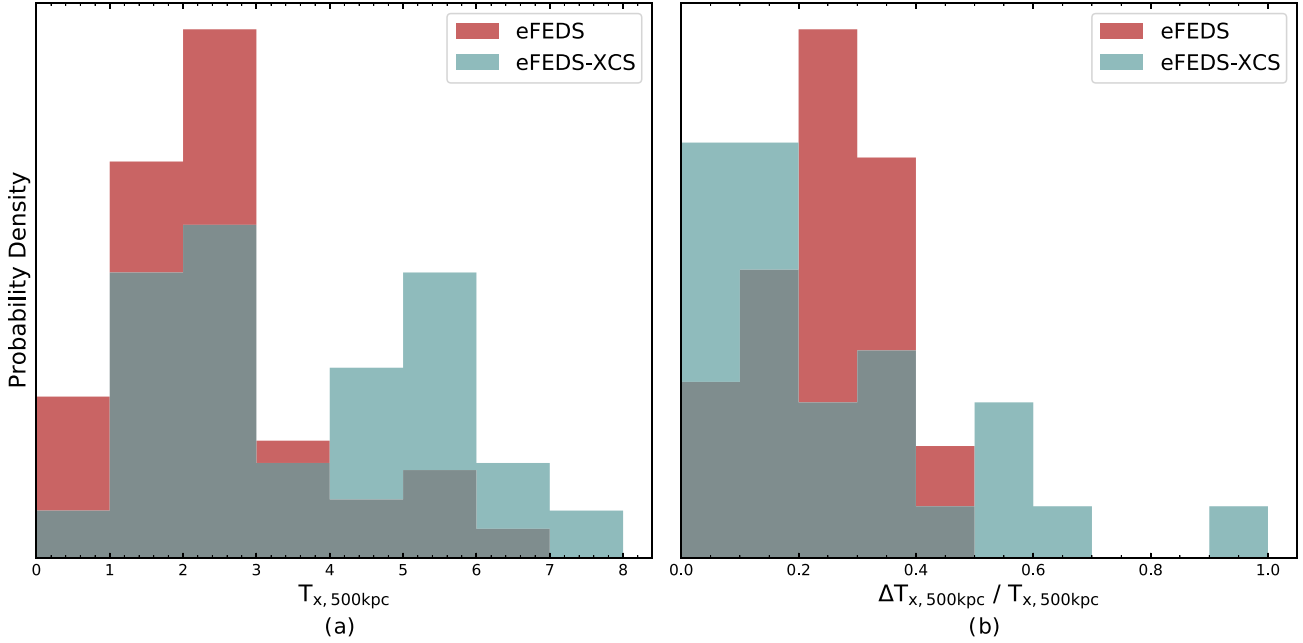
**Figure 11.** Temperature and fractional temperature error distributions of the eFEDS (red) and eFEDS-XCS (pale blue) samples, for measurements made within 500-kpc apertures, centred on eFEDS coordinates. The eFEDS sample plotted in red contains 95 *eROSITA* temperature measurements, and the eFEDS-XCS sample plotted in pale blue contains 28 *XMM* temperature measurements.
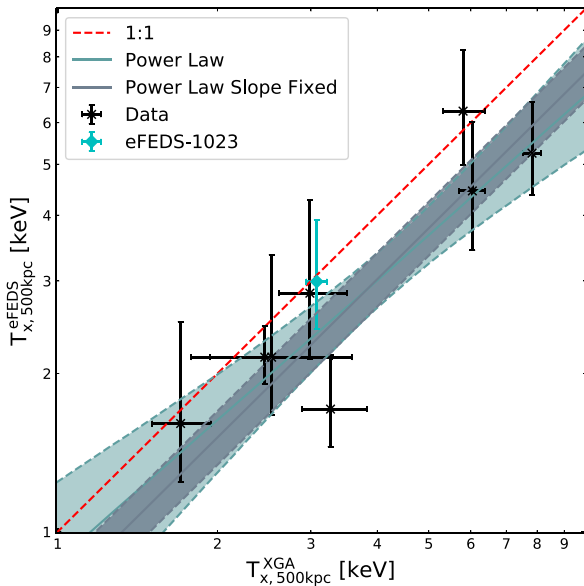


**Figure 12.** Comparison of eFEDS and XCS cluster temperatures within 500 kpc, centred on eFEDS coordinates. The pale blue line indicates the best-fitting power law (slope free to vary), with 68 per cent confidence levels given by the shaded region. The grey line indicates a power-law fit with a fixed slope of unity (with 68 per cent confidence levels given by the grey shaded region). Cyan diamond is for the split cluster discussed in Appendix B.

**Table 2.** The normalization, slope, and intrinsic scatter values of the fitted temperature calibration models for 500-kpc apertures.

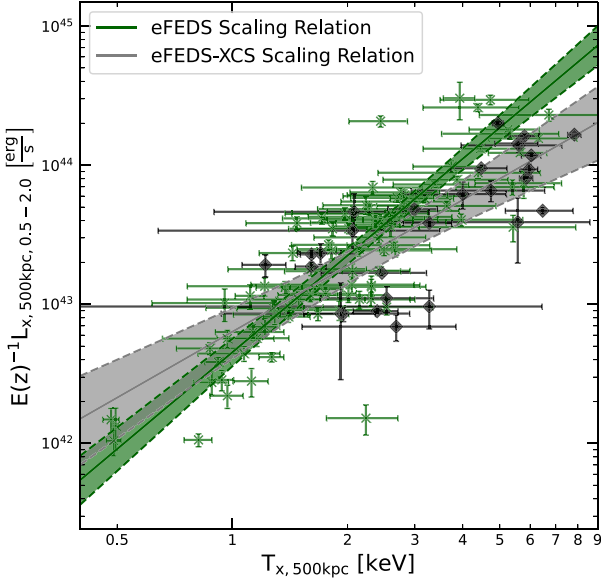| Calibration name | $A_{\mathrm{TT}}$ | $B_{\mathrm{TT}}$ | $\sigma_{T_{\mathrm{eROSITA}}|T_{\mathrm{XMM}}}$ |
|---|---|---|---|
| Power law | $0.88^{+0.37}_{-0.29}$ | $0.89^{+0.25}_{-0.24}$ | $0.04^{+0.06}_{-0.03}$ |
| Power-law fixed slope | $0.75^{+0.10}_{-0.08}$ | 1 | $0.04^{+0.05}_{-0.02}$ |

*Notes.* $A_{\mathrm{TT}}$ is the normalization, $B_{\mathrm{TT}}$ is the slope, and $\sigma_{T_{\mathrm{eROSITA}}|T_{\mathrm{XMM}}}$ is the intrinsic scatter.

in our respective methodologies. This may be supported by the analyses of Sanders et al. (2022) and Whelan et al. (2022), who generated temperature profiles from *eROSITA*, *XMM*, and *Chandra*, and found that *XMM* temperatures in their profiles were higher than *eROSITA*; the opposite of our findings. It is possible that a bias has been introduced by fitting a single-temperature plasma model to the spectra, as was explored by Schellenberger et al. (2015), or by a more basic analysis decision such as the choice of background region. We also measure temperatures using a simultaneous fit of all available *XMM* data, a mixture of PN, MOS1, and MOS2 spectra, which have have been shown to measure different temperatures (Schellenberger et al. 2015). The accuracy of the measured offset is also limited by small number statistics, as very few eFEDS selected clusters have both an *eROSITA* and an *XMM* temperature. However, we have provided evidence of an offset that requires further investigation to understand the mechanism behind it.

## 5 DISCUSSION

In this work we have presented a measurement of the temperature offset between *eROSITA* and *XMM* for a sample of galaxy clusters. Here we discuss potential impacts of this offset on the derived scaling relations and how the temperature calibration can be improved.

(on average) *eROSITA* measures a temperature ~25 per cent cooler than those measured by *XMM* for the same cluster.

As we have not re-analysed *eROSITA* data and measured our own *eROSITA* temperatures for the eFEDS-XCS cluster sample, the observed temperature offset could be the result of some mismatch

**Table 3.** The normalization, slope, and residual scatter values from the LIRA fits of the different data sets, for the $L_{X,0.5-2.0}^{500\,kpc}-T_X^{500\,kpc}$ scaling relation.

| Relation name | $A_{LT}$ | $B_{LT}$ | $\sigma_{L|T}$ |
|---|---|---|---|
| eFEDS | $1.03^{+0.09}_{-0.08}$ | $2.31^{+0.13}_{-0.13}$ | $0.19^{+0.03}_{-0.03}$ |
| eFEDS-XCS | $0.78^{+0.12}_{-0.11}$ | $1.58^{+0.22}_{-0.23}$ | $0.23^{+0.05}_{-0.04}$ |
| eFEDS-XCS Calibrated | $1.04^{+0.15}_{-0.14}$ | $1.76^{+0.25}_{-0.26}$ | $0.22^{+0.06}_{-0.04}$ |



**Figure 13.** Soft-band (0.5–2.0 keV) luminosity–temperature relations for the eFEDS and eFEDS-XCS samples. Properties measured within a 500-kpc fixed aperture centred on the eFEDS positions. eFEDS data points are green crosses and the model fit is green, and eFEDS-XCS data points are black diamonds with a grey model fit.



**Figure 14.** Corner plot of the 1σ and 2σ confidence contours of the $L_{x,0.5-2.0}^{500\,kpc}-T^{500\,kpc}$ relation parameters, for the eFEDS (green contours), eFEDS-XCS (grey contours), and eFEDS-XCS calibrated (blue contours) samples. The diagonal shows the posterior densities of each parameter.

## 5.1 Comparison of *eROSITA* and *XMM* X-ray scaling relations

We have explored the impact on X-ray scaling relations in light of the temperature offset measured in Section 4.4. We focus on the luminosity–temperature relation derived from eFEDS and XCS data. We use 28 eFEDS-XCS clusters with a successful 500-kpc *XMM* temperature ($T_X^{500\,kpc}$) and soft-band luminosity ($L_{X,0.5-2.0}^{500\,kpc}$) measurement (instead of limiting the analysis to the eight clusters used in Section 4.4 for temperature calibration), and all available eFEDS candidates with *eROSITA* measurements and compare the relations.

The $L_{X,0.5-2.0}^{500\,kpc}-L_X^{500\,kpc}$ relations for eFEDS (*eROSITA*) (grey points) and eFEDS-XCS (*XMM*) (green points) are shown in Fig. 13; the eFEDS relation uses data from 94 clusters. We fit both sets of data using a power law of the form:

$$\log\left(\frac{L_{X,0.5-2.0}^{500\,kpc}}{E(z)L_0}\right) = \log(A_{LT}) + B_{LT}\log\left(\frac{T_X^{500\,kpc}}{T_0}\right) \pm \sigma_{L|T}, \quad (2)$$
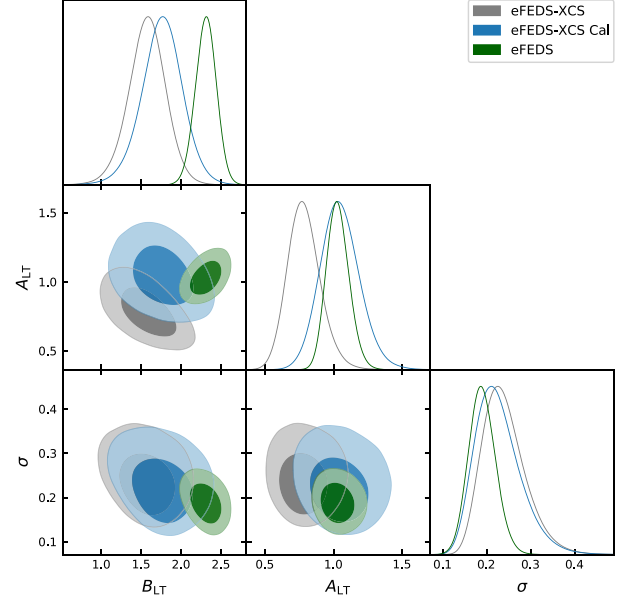
where $A_{LT}$ denotes the normalization, $B_{LT}$ denotes the slope, and $\sigma_{L|T}$ denotes the intrinsic scatter of the relation. We calculate $E(z)$ using the redshift supplied in the eFEDS catalogue and our chosen concordance cosmology. The fits are performed using the LIRA package. We set normalization values for luminosity and temperature to approximate median eFEDS values; $L_0 = 3.0 \times 10^{43}$ erg s$^{-1}$ and $T_0 = 2.3$ keV.

Fig. 13 shows the best-fitting relations using the eFEDS (green line) and eFEDS-XCS (grey line) samples, respectively. The best-fitting values are given in Table 3, with their distributions illustrated in Fig. 14. While the distributions highlight that the parameters of the relation are consistent within their 2σ contours, the difference in the central value of the slope warrants further discussion.

We explore whether this difference can be reduced by accounting for the observed temperature offset found in Section 4.4. We measure a third version of the scaling relation, designed to test the effect of

the temperature calibration quantified in Section 4.4. We determine a 'calibrated' luminosity–temperature relation by using the power-law model (with the slope free to vary), with parameter values provided in Table 2, to convert the eFEDS-XCS *XMM* temperature values into predicted *eROSITA* values.

Fig. 15 shows the model fits for all three relations (with data points omitted for clarity), and shows that the eFEDS-XCS calibrated scaling relation has a steepened slope and increased normalization when compared to the original eFEDS-XCS relation. Fig. 14 shows a shift of the contours and distributions (the eFEDS-XCS calibrated parameters are given by the blue contours) towards eFEDS (blue contours). The normalization of the calibrated eFEDS-XCS relation is fully consistent with the eFEDS relation, with the tension in the measured slopes reduced.

Bahar et al. (2022) have constructed a variety of scaling relations using eFEDS *eROSITA* properties measured within $R_{500}$, including luminosity–temperature relations. They found their relation to be in agreement with past work using *XMM*, though with a slightly steeper slope than the XXL (Giles et al. 2016) result. Our relations indicate a larger difference in slope, but we do not account for selection effects, we use properties measured within 500 kpc rather than $R_{500}$, and our analyses are not completely consistent with eFEDS as has been discussed elsewhere.
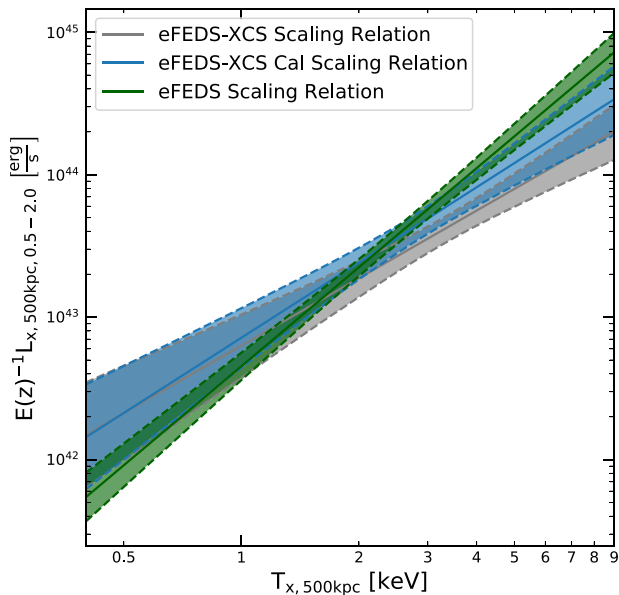
**Figure 15.** Soft-band luminosity–temperature relations for eFEDS, eFEDS-XCS, and calibrated eFEDS-XCS. Properties measured within a 500-kpc fixed aperture centred on the eFEDS positions.

### 5.2 Future work to improve the calibration of the *XMM* to *eROSITA* temperature offset

The measured temperature discrepancy described in Section 4.4 and shown in Fig. 12 is based on only eight sets of measurements, of which only three are more than $1\sigma$ from the one-to-one relation. Further investigation is required to quantify the level of a temperature offset between the *XMM* and *eROSITA*. For this, we plan three complementary approaches:

(i) Re-analyse the eFEDS cluster candidate observations using an identical spectroscopic methodology to the *XMM* analysis. This way, we will have control of all aspects of the analysis, including which regions are used to mask the observations for spectrum generation (see a related discussion in Appendix B). This will be done for all 94 clusters in the eFEDS luminosity–temperature analysis (Fig. 13), which includes the eight clusters featured in Fig. 12.

(ii) Propose *XMM* follow-up observations of a representative sample of eFEDS clusters with robustly (i.e. percentage error less than 25 per cent) measured *eROSITA* temperatures. There are 43 such examples in the eFEDS data release that are not already included in the analysis shown in Fig. 12. We will preferentially select clusters that fill gaps at the high- and low-temperature ends, to better constrain a temperature-dependent slope in the calibration relation (if one exists).

(iii) Repeat the analysis herein after the next *eROSITA*-DE data release (due in Q4 2022[7]). This will cover the whole Southern sky (red area in Fig. 16) and thus overlap with many more archival *XMM* observations than did eFEDS (grey points and regions in Fig. 16). The next data release will have an exposure time eight times less shorter than eFEDS (one pass), but, with ∼150 times the area, we can still expect it to yield roughly 1000 robust temperature measurements.

---

[7] *eROSITA*-DE Data Release Schedule.

## 6 SUMMARY

In this work we have performed the first comparison between cluster properties measured by the eFEDS survey and those measured by *XMM* surveys, both directly and for ensembles of clusters. A comparison of XXL-100-GC and the eFEDS optically confirmed sample indicated that the two samples have very similar redshift distributions, that XXL-100-GC contained proportionally more temperature measurements above 3.5 keV, and that XXL-100-GC temperatures are, on average, better constrained than eFEDS temperatures (14 per cent versus 25 per cent average percentage uncertainties, respectively).

We have located and analysed eFEDS cluster candidates that have a counterpart in an *XMM* observation; as part of this process, we visually inspected eFEDS cluster candidates that are within an *XMM* observation and rejected any that had no ICM emission at the eFEDS coordinates, had obviously contaminated ICM emission, or too low-quality *XMM* data. The eFEDS-*XMM* sample contains 62 eFEDS cluster candidates that have been observed by *XMM*, and the eFEDS-XCS subsample contains the 37 clusters that pass our visual inspection (Table 1). During visual inspection, we found that 10 candidates (Table A1) did not have sufficient *XMM* data to confirm or deny a cluster, 4 had X-ray flux contamination (Section 3.4, Table A3), and 11 were sample contaminants (Section 3.3, Table A2). We found that the majority of eFEDS-*XMM* candidates had a longer exposure time (at their eFEDS position) in *XMM* than in eFEDS. We also found that the majority of eFEDS centroid positions for the eFEDS-XCS sample are within 100 kpc (at the eFEDS redshift) of the XCS centroid positions (for clusters with an XCS match), though some outliers exist due to low signal-to-noise eFEDS data.

Our visual inspections of the eFEDS cluster candidates that fall on an *XMM* field (using *eROSITA*, *XMM*, SDSS and HCS images) have shown that there are some aspects of *eROSITA*'s source finding and confirmation steps that can introduce spurious sources into their catalogues, which, in turn, could impact their cosmological analyses. Our inspection process finds that the eFEDS-*XMM* sample is (at minimum) ∼18 per cent contaminated, and that optically confirmed sample is ∼9 per cent (∼6 per cent if made more consistent with the eFEDS sample selection method) contaminated. This is consistent with predictions from simulations (Comparat et al. 2020) and eFEDS measured values (Klein et al. 2022).

We have presented comparisons between cluster luminosities and temperatures measured with *eROSITA* and *XMM*. Our analysis finds excellent agreement between soft-band luminosities measured by eFEDS and XCS for the eFEDS-XCS sample (Section 4.2), which is very encouraging for future eRASS cosmology analyses. Such analyses will rely almost exclusively on mass–luminosity relations (such as the recent eFEDS-HSC work; Chiu et al. 2021), as even full-depth eRASS will not be able to measure temperatures for enough galaxy clusters to use mass–temperature relations for cosmology. An ensemble cluster comparison was performed (Section 4.3) between the whole eFEDS cluster candidate sample (that had successful temperature/luminosity measurements), and the eFEDS-XCS sample (that had successful temperature/luminosity measurements). It showed similar results to the XXL-100-GC comparison, with a greater fraction of *XMM* temperature measurements being above 4 keV than eFEDS temperatures, and better average temperature constraints for *XMM* measurements.

A discrepancy between cluster temperatures measured by eFEDS and XCS has been found and quantified (Section 4.4), with *eROSITA* temperatures being (on average) $25 \pm 9$ per cent cooler than those measured by *XMM* for the same cluster. This could hint at the need for
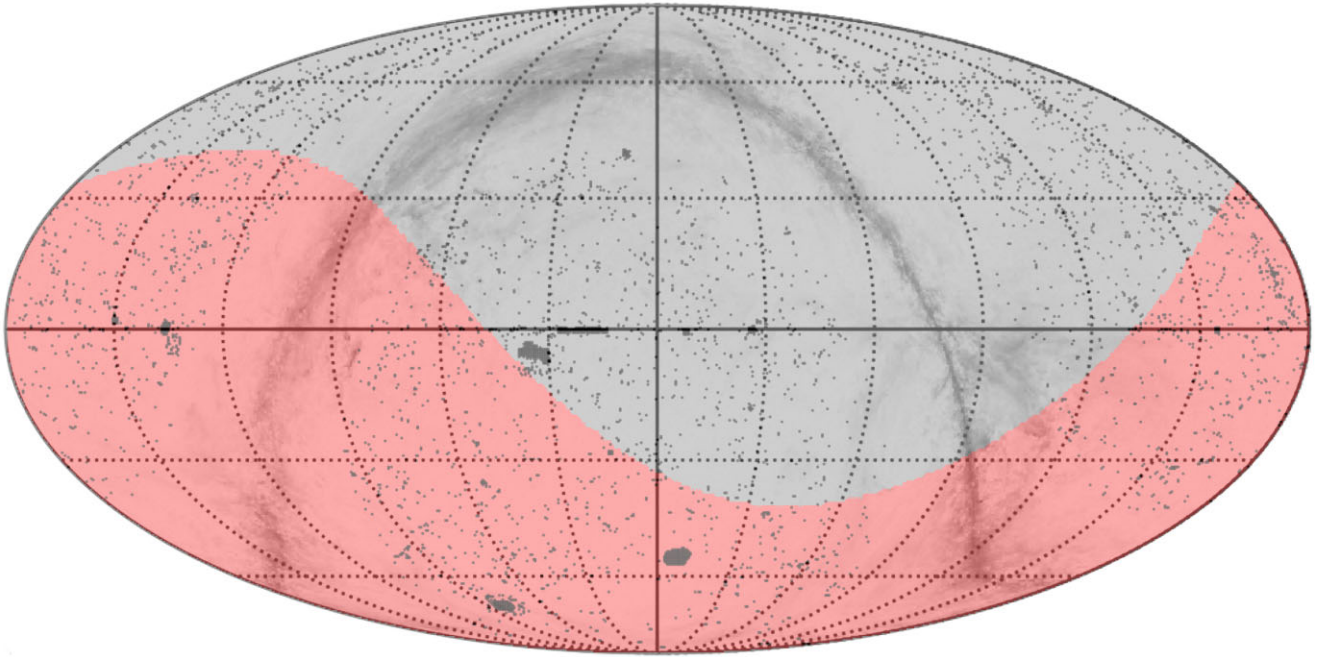
**Figure 16.** Distribution of *XMM* observations projected over the sky, indicated by grey points. The eRASS-DE half of the sky is highlighted by the red region. The background is the Planck-DustPol (Padovani et al. 2012) map, available for download on NASA's Lambda service.

a calibration function between the *eROSITA* and *XMM* telescopes (as has been necessary between *XMM* and *Chandra*). Several variables need to be better controlled before we can definitively state that the observed discrepancy is entirely due to a required temperature calibration. Alternative explanations including biases introduced by fitting a single-temperature plasma model to a multiphase emission, or a combination of analysis choices, are made more likely by initial studies of temperature profiles finding *eROSITA* temperatures to be higher than *XMM* temperatures.

We also fit and compare luminosity–temperature scaling relations using data from the eFEDS catalogue and *XMM* data for the eFEDS-XCS sample, using them to compare scaling relations measured with *eROSITA* and *XMM* data. This has particular relevance for anyone wishing to use an *XMM*-generated scaling relation in an *eROSITA* analysis, or vice versa, as we find a distinct tension between scaling relations from the eFEDS and eFEDS-XCS samples. We also generate a second, calibrated, eFEDS-XCS scaling relation that is in better agreement with the eFEDS relation; normalization becomes entirely consistent, and the slope measurement tension is reduced. This again may suggest that a temperature scaling between *XMM* and *eROSITA* is necessary. It is likely, however, that a large part of the observed tension between the scaling relations is due to selection effects.

Our comparisons have shown that we can expect a great deal of useful data from the full eRASS catalogues, and that *XMM–Newton* still has a significant part to play as follow-up instrument. Its archive of 20 yr worth of observations is still extremely valuable to the *eROSITA* team, and the X-ray astronomy community as a whole, and there will be many excellent opportunities for synergies between the two telescopes.

## ACKNOWLEDGEMENTS

## DATA AVAILABILITY

The data underlying this paper were accessed from the eROSITA Early Data Release site, and the *XMM* science archive. The derived data underlying this study are available in this paper and in its online supplementary material.

## REFERENCES

Ahumada R. et al., 2020, ApJS, 249, 3
Aihara H. et al., 2018, PASJ, 70, S4
Aihara H. et al., 2019, PASJ, 71, 114
Arnaud K. A., 1996, in Jacoby G. H., Barnes J., eds, ASP Conf. Ser. Vol. 101, Astronomical Data Analysis Software and Systems V. Astron. Soc. Pac., San Francisco, p. 17
Asplund M., Grevesse N., Sauval A. J., Scott P., 2009, ARA&A, 47, 481
Astropy Collaboration et al., 2013, A&A, 558, A33
Astropy Collaboration et al., 2018, AJ, 156, 123
Bahar Y. E. et al., 2022, A&A, 661, A7
Bhargava S. et al., 2020, MNRAS, 497, 656
Blanton M. R. et al., 2017, AJ, 154, 28
Boller T. et al., 2021, A&A, 647, A6
Brunner H. et al., 2018, in den Herder J.-W. A., Nikzad S., Nakazawa K., eds, Society of Photo-Optical Instrumentation Engineers (SPIE) Conference Series, Vol. 10699, Space Telescopes and Instrumentation 2018: Ultraviolet to Gamma Ray. p. 106995G
Brunner H. et al., 2021, A&A, 661, 25
Chiu I.-N. et al., 2021, A&A, 661, 41
Comparat J. et al., 2020, Open J. Astrophys., 3, 13
Driver S. P. et al., 2011, MNRAS, 413, 971
Farahi A. et al., 2019, Nat. Commun., 10, 2504
Flesch E. W., 2021, preprint (arXiv:2105.12985)
Gabriel C. et al., 2004, in Ochsenbein F., Allen M. G., Egret D., eds, ASP Conf. Ser. Vol. 314, Astronomical Data Analysis Software and Systems (ADASS) XIII. Astron. Soc. Pac., San Francisco, p. 759
Giles P. A. et al., 2016, A&A, 592, A3
Giles P. A. et al., 2022, preprint (arXiv:2202.11107)
Harris C. R. et al., 2020, Nature, 585, 357
HI4PI Collaboration et al., 2016, A&A, 594, A116
Hitomi Collaboration et al., 2016, Nature, 535, 117
Hunter J. D., 2007, Comput. Sci. Eng., 9, 90
Klein M. et al., 2018, MNRAS, 474, 3324
Klein M. et al., 2022, A&A, 661, A4
Koulouridis E. et al., 2021, A&A, 652, A12
Lewis A., 2019, preprint (arXiv:1910.13970)
Liu A. et al., 2021a, A&A, 661, 25
Liu T. et al., 2022, A&A, 661, A5
Lloyd-Davies E. J. et al., 2011, MNRAS, 418, 14
McKinney W., 2010, in van der Walt S., Millman J., eds, Proceedings of the 9th Python in Science Conference, p. 56
Migkas K., Schellenberger G., Reiprich T. H., Pacaud F., Ramos-Ceja M. E., Lovisari L., 2020, A&A, 636, A15
Pacaud F. et al., 2016, A&A, 592, A2
Padovani M. et al., 2012, A&A, 543, A16
Pfeifle R. W. et al., 2019, ApJ, 875, 117
Pierre M. et al., 2016, A&A, 592, A1
Pillepich A., Porciani C., Reiprich T. H., 2012, MNRAS, 422, 44
Predehl P. et al., 2021, A&A, 647, A1
Romer A. K., Viana P. T. P., Liddle A. R., Mann R. G., 1999, preprint (arXiv:astro-ph/9911499)
Sanders J. S. et al., 2021, A&A, 661, 27
Sanders J. S. et al., 2022, A&A, 661, A36
Schellenberger G., Reiprich T. H., 2017, MNRAS, 471, 1370
Schellenberger G., Reiprich T. H., Lovisari L., Nevalainen J., David L., 2015, A&A, 575, A30
Sereno M., 2016a, Astrophysics Source Code Library, record ascl:1602.006
Sereno M., 2016b, MNRAS, 455, 2149
Smith R. K., Brickhouse N. S., Liedahl D. A., Raymond J. C., 2001, ApJ, 556, L91
Taylor M. B., 2005, in Shopbell P., Britton M., Ebert R., eds, ASP Conf. Ser. Vol. 347, Astronomical Data Analysis Software and Systems XIV. Astron. Soc. Pac., San Francisco, p. 29
The Pandas Development Team, 2020, pandas-dev/pandas: Pandas
Turner D. J., Giles P. A., Romer A. K., Korbina V., 2022, preprint (arXiv:2202.01236)
Vikhlinin A. et al., 2009, ApJ, 692, 1060
Whelan B. et al., 2022, A&A, 663, 171
Wilms J., Allen A., McCray R., 2000, ApJ, 542, 914

## APPENDIX A: EXCLUDED CLUSTER CANDIDATES

This section details the eFEDS-*XMM* X-ray cluster candidates that were not included in eFEDS-XCS sample, as discussed in Section 3. Basic information about the samples used in this work is available in Table 1. Table A1 contains candidates that were not included due to

**Table A1.** eFEDS-*XMM* galaxy cluster candidates excluded from further analysis due to one or more *XMM–Newton* data quality issues.

| eFEDS ID | RA | Dec. | $z$ | EL | DL | Notes |
|---|---|---|---|---|---|---|
| 8094[†] | 133.644 | − 1.677 | 0.595 | 13.56 | 38.71 | On the edge of the *XMM* field of view. |
| 7700 | 133.669 | − 2.159 | 0.472 | 6.95 | 32.39 | On the edge of the *XMM* field of view. |
| 1797[†] | 133.876 | − 1.11 | 0.754 | 40.55 | 74.33 | On the edge of the *XMM* field of view (*eROSITA* image confirms presence of extended source). |
| 11836[†] | 135.272 | − 1.424 | 0.405 | 17.78 | 29.38 | On the edge of the *XMM* field of view, and the *XMM* observation is shallow (1023-s exposure at the eFEDS coordinates). The *eROSITA* image confirms presence of an extended source. |
| 9877[†] | 136.04 | 0.642 | 0.311 | 12.22 | 18.62 | Low signal-to-noise *XMM* image (7489-s exposure at the eFEDS coordinates) that has been affected by flaring. |
| 2757[†] | 134.756 | 1.114 | 0.162 | 33.65 | 97.42 | Low signal-to-noise *XMM* image (6870-s exposure at the eFEDS coordinates). |
| 5858 | 136.687 | 1.19 | 0.441 | 9.78 | 60.28 | Low signal-to-noise *XMM* image (15 020-s exposure at the eFEDS coordinates). *eROSITA* image confirms presence of extended source. |
| 2074[†] | 136.971 | 1.569 | 0.163 | 9.43 | 17.90 | Low signal-to-noise *XMM* image (5331-s exposure at the eFEDS coordinates). |
| 11837[†] | 138.201 | 0.413 | 0.308 | 7.06 | 17.43 | Low signal-to-noise *XMM* image (29 479-s exposure at the eFEDS coordinates) that has been affected by flaring. The *eROSITA* image confirms presence of an extended source. |
| 1376[†] | 133.23 | − 1.627 | 0.343 | 7.35 | 14.90 | *XMM* data too shallow for confirmation. The *eROSITA* and SDSS data indicate a likely cluster, but eFEDS coordinate is offset from the extended emission and SDSS galaxies. |

*Notes.* The EL and DL columns correspond to the extent likelihood (EXT_LIKE) and detection likelihood (DET_LIKE) columns in the eFEDS catalogue. [†] indicates that the candidate was present in the optically confirmed sample from Klein et al. (2022).

**Table A2.** eFEDS-*XMM* galaxy cluster candidates classed as contaminants during our visual inspection of *XMM*, *eROSITA*, and SDSS images.

| eFEDS ID | RA | Dec. | $z$ | EL | DL | Notes |
|---|---|---|---|---|---|---|
| 1644[†] | 130.396 | 1.031 | 0.507 | 16.55 | 139.61 | Blend: In *XMM* image two point sources are detected, due to *XMM*'s smaller PSF effect. The source is the target of the *XMM* observation and is associated with an interacting pair of active galaxies (see Fig. 5). |
| 3334[†] | 130.508 | 0.995 | 0.087 | 7.52 | 9.95 | Spurious: There is not an X-ray source at this location in either the *XMM* or *eROSITA* images, nor do there appear to be any associated galaxies in the SDSS/HSC images. |
| 8602[†] | 132.593 | 0.269 | 0.196 | 13.40 | 18.24 | Fragmented: The ICM emission from a single cluster that has been classified as coming from two eFEDS candidates, ID 8602 and 1023. |
| 5909[†] | 133.83 | −1.721 | 0.365 | 12.90 | 42.53 | Spurious: There is an X-ray source at the eFEDS candidate location, but it is a defined as point source by XCS in the higher signal-to-noise *XMM data*. There are no associated galaxies in the SDSS or HSC images. |
| 8922[†] | 134.067 | −1.663 | 0.514 | 10.56 | 22.47 | Spurious: In eFEDS, this is a spurious detection of the outskirts of the emission from an X-ray bright spiral galaxy. In the higher resolution *XMM* image, there is no source at this location. |
| 9463 | 136.753 | 1.176 | 0.799 | 10.29 | 23.07 | Blend: In the higher signal-to-noise (18 501-s exposure) *XMM* image, two point sources detected. |
| 13484 | 136.766 | 1.132 | 0.307 | 7.90 | 12.57 | Spurious: There is no obvious extended X-ray emission in either the *eROSITA* or *XMM* data. There are no associated galaxies in the SDSS or HSC images. |
| 13299 | 138.691 | 4.439 | 0.348 | 14.78 | 17.75 | Spurious: In eFEDS, this is a spurious detection of the outskirts of the emission from an X-ray bright star. |
| 11754 | 140.018 | 1.007 | 0.033 | 19.95 | 35.88 | Spurious: Spurious detection in outskirts of nearby eFEDS candidate ID 150 ($z = 0.017$). |
| 5702 | 130.295 | 0.867 | 0.415 | 7.13 | 39.44 | Spurious: In the higher signal-to-noise (130 445-s exposure) *XMM* image, a point source is detected that appears to be associated with a blue (i.e. likely AGN) object in the SDSS and HSC images. |
| 6840 | 135.597 | 1.868 | 0.561 | 6.75 | 43.23 | Spurious: In the *XMM* image, XCS detects a point source that appears to be associated with a blue (i.e. likely AGN) object in the SDSS and HSC images. |

*Notes*. The EL and DL columns correspond to the extent likelihood (EXT_LIKE) and detection likelihood (DET_LIKE) columns in the eFEDS catalogue. [†] indicates that the candidate was present in the optically confirmed sample from Klein et al. (2022).

**Table A3.** eFEDS-*XMM* galaxy cluster candidates that appear to be galaxy clusters whose X-ray emission is significantly contaminated by another source.

| eFEDS ID | RA | Dec. | $z$ | EL | DL | Notes |
|---|---|---|---|---|---|---|
| 16370[†] | 134.098 | −1.604 | 0.425 | 11.86 | 17.74 | eFEDS candidate coincident with a collection of galaxies in SDSS/HSC; however, the X-ray emission is contaminated by the low-redshift spiral galaxy. |
| 150[†] | 140.009 | 1.039 | 0.017 | 179.59 | 1049.64 | SDSS/HSC indicates the presence of a group of galaxies; however, the X-ray emission originates primarily from the central galaxy. |
| 3133[†] | 140.649 | −0.412 | 0.055 | 30.21 | 49.42 | SDSS/HSC indicates the presence of a group of galaxies; however, the X-ray emission originates primarily from the central galaxy. |
| 3008[†] | 130.451 | 0.82 | 0.078 | 16.78 | 80.87 | SDSS/HSC indicates the presence of a group of galaxies; however, the X-ray emission originates primarily from the central galaxy. |

*Notes*. The EL and DL columns correspond to the extent likelihood (EXT_LIKE) and detection likelihood (DET_LIKE) columns in the eFEDS catalogue. [†] indicates that the candidate was present in the optically confirmed sample from Klein et al. (2022).

the low quality of the *XMM* data available, Table A3 contains galaxy clusters whose X-ray emission has been significantly contaminated by another X-ray source and as such were not included in the eFEDS-XCS sample. Table A2 contains sample contaminants that were not included in the eFEDS-XCS sample (see Section 3.2).

## APPENDIX B: EFEDS CANDIDATE 1023

This galaxy cluster has been been split into two sources by the eFEDS source finder; a visual inspection confirmed a single extended X-ray source (in both *eROSITA* and *XMM* images) and a single projected distribution of red galaxies (Section 3.3.3). XCS also detected this as a single extended source.

One of the two eFEDS catalogue entries that make up this cluster has measured *eROSITA* $T_X$ and $L_X$ values. These values will be impacted by the masking of emission from the other component.

Therefore, it would not be appropriate to include those values in the comparisons presented in Figs 10 or 12.

However, we have attempted to mimic the *eROSITA* values using *XMM* data. This involves manually adding a region to be excluded when the *XMM* spectra are generated. This region is centred on the eFEDS X-ray candidate catalogue coordinates for eFEDS-8602, and uses the 'extent' value for that candidate published in the optical counterpart catalogue as the radius of the new exclusion region. Doing this, we find the *XMM* determined $L_X$ and $T_X$ values are consistent with those presented in Liu et al. (2021a); see Figs 10 and 12 (cyan diamond).

## APPENDIX C: EFEDS-XCS DATA AND MEASUREMENTS

In Table C1, we present information on the *XMM* data that were used for each eFEDS-XCS cluster, including the unique *XMM*

observation identifier and which instruments had usable data. We also include information on which instruments of which observations were contributed to the final luminosity and temperature measurements of each eFEDS-XCS cluster. In Table C2, we present temperature and luminosity values measured for the clusters in the eFEDS-XCS sample. We use XGA to generate spectra and run XSPEC fits for these clusters. The fitting procedure is discussed in more detail in Section 4.1. All measurements are centred on the eFEDS coordinates from the X-ray cluster candidate catalogue, with redshift information also taken from that catalogue.

**Table C1.** The *XMM* data used in the analysis of the eFEDS-XCS sample .

| eFEDS ID | ObsID | $PN_A$ | $MOS1_A$ | $MOS2_A$ | $PN_{500\,kpc}$ | $MOS1_{500\,kpc}$ | $MOS2_{500\,kpc}$ |
|---|---|---|---|---|---|---|---|
| 6605 | 0202940101 | T | T | T | F | F | F |
|  | 0202940201 | T | T | T | T | T | T |
| 144 | 0650381601 | T | T | T | T | T | T |
| 7831 | 0784350101 | T | T | T | T | T | T |
| 1023 | 0761730501 | T | F | T | T | – | T |
| 6125 | 0761730501 | T | F | T | T | – | T |
| 339 | 0655340137 | T | T | T | T | T | T |
| 4810 | 0655340137 | T | T | T | T | F | F |
| 1458 | 0655340135 | T | T | T | T | T | T |
| 2079 | 0651170301 | T | T | T | T | T | T |
| 569 | 0783881001 | T | T | T | T | T | T |
| 1385 | 0783881001 | T | F | T | T | – | T |
| 8857 | 0725290142 | T | T | T | – | – | – |
| 3171 | 0725300134 | T | F | T | F | – | T |
|  | 0725290144 | T | T | T | T | T | F |
|  | 0725290145 | T | F | T | T | – | T |
| 8881 | 0725290139 | T | T | T | F | F | F |
|  | 0725290146 | T | T | T | T | F | T |
| 1104 | 0655340160 | T | T | T | T | F | T |
|  | 0804410201 | T | T | T | T | T | T |
| 4232 | 0655340160 | T | T | T | F | F | F |
|  | 0804410201 | T | T | T | T | T | T |
| 5655 | 0725300158 | T | T | T | T | T | F |
|  | 0725300159 | T | F | T | T | – | T |
|  | 0725300136 | T | T | F | T | F | – |
| 1712 | 0725300140 | T | T | F | T | T | – |
|  | 0725300132 | T | T | T | T | F | F |
|  | 0725300131 | T | T | T | F | F | T |
| 5774 | 0725300157 | T | T | T | – | – | – |
|  | 0725310131 | T | T | T | – | – | – |
| 3590 | 0725310152 | T | T | T | T | F | F |
|  | 0725300160 | T | F | T | F | – | F |
| 12660 | 0725290131 | T | T | T | T | T | T |
|  | 0725290154 | T | T | T | F | T | T |
| 3585 | 0725310149 | T | T | T | T | F | F |
|  | 0725310150 | T | T | T | T | F | T |
|  | 0725310131 | T | F | F | T | – | – |
| 5170 | 0725300152 | T | F | T | T | – | F |
|  | 0725300153 | T | T | T | T | F | F |
| 9359 | 0725300145 | T | F | T | T | – | T |
|  | 0725300146 | T | T | T | T | F | F |
| 3259 | 0725300144 | T | T | T | T | T | T |
|  | 0725300151 | T | T | T | F | F | T |
| 7086 | 0725310133 | T | F | F | – | – | – |
|  | 0725310147 | T | F | T | – | – | – |
|  | 0725310148 | T | T | T | – | – | – |
|  | 0725310157 | F | F | T | – | – | – |
|  | 0402780801 | T | T | T | – | – | – |
| 5219 | 0725310158 | T | T | T | T | F | F |
|  | 0725310147 | T | F | F | T | – | – |
|  | 0725310159 | T | T | T | T | F | F |
| 7084 | 0725310157 | T | T | T | – | – | – |
| 885 | 0725310142 | T | T | T | T | T | T |
|  | 0725310141 | T | F | T | T | – | T |

**Table C1** – *continued*

| eFEDS ID | ObsID | PN$_A$ | MOS1$_A$ | MOS2$_A$ | PN$_{500\,kpc}$ | MOS1$_{500\,kpc}$ | MOS2$_{500\,kpc}$ |
|---|---|---|---|---|---|---|---|
| 2004 | 0800400501 | T | F | T | T | – | T |
| 3523 | 0800400501 | T | T | T | F | T | T |
| 372 | 0602830401 | T | F | F | T | – | – |
| 4253 | 0602830401 | T | F | T | F | – | T |
| 534 | 0804410101 | T | T | T | T | T | T |
| | 0650381801 | T | T | T | T | T | T |
| 100 | 0804410501 | T | T | T | T | T | T |
| 857 | 0823710301 | T | T | T | T | T | T |
| 12565 | 0802220601 | T | F | F | – | – | – |

*Notes*. Individual clusters denoted by their unique eFEDS ID. ObsID contains the unique identifier(s) of the *XMM* observation(s) used. T denotes true, F denotes false, – denotes that either no successful spectral fit was performed, or the data for that cameras were not available. Columns with a subscript A (e.g. PN$_A$) indicate whether that instrument is available for an ObsID. Columns with a subscript radius (e.g. PN$_{500\,kpc}$) indicate whether that instrument's data contributed to the final XSPEC fit from which we extract temperature and luminosity information.

**Table C2.** eFEDS-XCS galaxy cluster XGA measured values, RA, Dec., and redshift are taken from the eFEDS X-ray cluster candidate catalogue.

| eFEDS ID | RA | Dec. | $z$ | $T^{XGA}_{x,500\,kpc}$ | $L^{XGA,52}_{x,500\,kpc}$ | $L^{XGA,bol}_{x,500\,kpc}$ |
|---|---|---|---|---|---|---|
| 6605 | 130.353 | 0.777 | 0.41 | $1.61^{+0.16}_{-0.13}$ | $2.32^{+0.16}_{-0.17}$ | $4.81^{+0.46}_{-0.41}$ |
| 144 | 131.37 | 3.461 | 0.33 | $5.8^{+0.59}_{-0.48}$ | $19.18^{+0.84}_{-0.67}$ | $67.1^{+3.88}_{-3.88}$ |
| 7831 | 132.272 | 2.243 | 0.4 | $1.61^{+0.1}_{-0.11}$ | $2.82^{+0.21}_{-0.15}$ | $5.87^{+0.44}_{-0.43}$ |
| 1023$^\dagger$ | 132.616 | 0.251 | 0.2 | $3.08^{+0.14}_{-0.13}$ | $3.55^{+0.04}_{-0.05}$ | $9.29^{+0.25}_{-0.22}$ |
| 6125 | 132.627 | 0.558 | 0.19 | $2.39^{+0.33}_{-0.31}$ | $0.98^{+0.05}_{-0.05}$ | $2.35^{+0.2}_{-0.18}$ |
| 339 | 133.071 | −1.025 | 0.46 | $5.57^{+0.81}_{-0.63}$ | $18.3^{+0.71}_{-0.76}$ | $62.82^{+4.09}_{-6.48}$ |
| 4810 | 133.13 | −1.208 | 0.55 | $2.06^{+2.12}_{-0.72}$ | $4.56^{+1.06}_{-1.85}$ | $10.14^{+3.84}_{-4.1}$ |
| 1458 | 133.554 | −2.357 | 0.38 | $4.47^{+0.78}_{-0.72}$ | $11.59^{+0.53}_{-0.75}$ | $35.63^{+3.34}_{-4.39}$ |
| 2079 | 133.696 | −1.359 | 0.35 | $3.27^{+0.56}_{-0.38}$ | $4.59^{+0.23}_{-0.27}$ | $12.23^{+0.86}_{-0.98}$ |
| 569 | 134.086 | 1.78 | 0.72 | $4.94^{+0.16}_{-0.16}$ | $29.96^{+0.55}_{-0.44}$ | $96.29^{+2.02}_{-1.94}$ |
| 1385 | 134.113 | 1.705 | 0.73 | $6.47^{+1.49}_{-1.11}$ | $7.06^{+0.4}_{-0.37}$ | $26.2^{+2.66}_{-3.5}$ |
| 8857 | 134.658 | 1.449 | 0.75 | – | – | – |
| 3171 | 135.269 | 1.279 | 0.25 | $1.7^{+0.24}_{-0.2}$ | $2.64^{+0.26}_{-0.63}$ | $5.69^{+0.76}_{-1.3}$ |
| 8881 | 135.314 | 0.844 | 0.31 | $3.27^{+4.56}_{-1.79}$ | $1.13^{+0.34}_{-0.36}$ | $3.02^{+1.2}_{-1.7}$ |
| 1104 | 135.372 | −1.648 | 0.31 | $5.96^{+0.32}_{-0.32}$ | $10.94^{+1.11}_{-0.81}$ | $38.75^{+4.67}_{-4.06}$ |
| 4232 | 135.443 | −1.632 | 0.29 | $1.95^{+0.53}_{-0.3}$ | $0.99^{+0.1}_{-0.14}$ | $2.19^{+0.36}_{-0.33}$ |
| 5655 | 135.735 | 1.774 | 0.12 | $0.97^{+0.11}_{-0.12}$ | $0.02^{+0.11}_{-0.02}$ | $0.04^{+0.19}_{-0.04}$ |
| 1712 | 135.74 | 0.805 | 0.52 | $2.08^{+1.74}_{-0.63}$ | $6.12^{+2.32}_{-1.85}$ | $13.68^{+4.61}_{-4.53}$ |
| 5774 | 136.036 | 1.432 | 0.84 | – | – | – |
| 3590 | 136.078 | 2.112 | 0.81 | $4.99^{+8.64}_{-2.3}$ | $10.17^{+1.35}_{-3.57}$ | $32.84^{+7.6}_{-13.35}$ |
| 12660 | 136.08 | −1.077 | 0.31 | $2.68^{+1.51}_{-0.81}$ | $0.81^{+0.21}_{-0.14}$ | $2.01^{+0.55}_{-0.47}$ |
| 3585 | 136.42 | 1.539 | 0.64 | $4.0^{+1.46}_{-0.94}$ | $8.81^{+2.0}_{-1.89}$ | $25.52^{+6.27}_{-6.63}$ |
| 5170 | 136.473 | 0.379 | 0.37 | $1.22^{+0.14}_{-0.18}$ | $2.33^{+0.38}_{-0.46}$ | $4.42^{+0.74}_{-0.94}$ |
| 9359 | 136.502 | −0.423 | 0.3 | $1.92^{+1.46}_{-0.51}$ | $1.0^{+0.66}_{-0.67}$ | $2.2^{+1.89}_{-1.4}$ |
| 3259 | 136.504 | 0.015 | 0.2 | $2.53^{+1.06}_{-0.59}$ | $1.22^{+0.33}_{-0.19}$ | $2.96^{+0.87}_{-0.68}$ |
| 7086 | 136.654 | 1.148 | 0.79 | – | – | – |
| 5219 | 136.977 | 0.961 | 0.74 | $4.74^{+2.17}_{-1.44}$ | $9.92^{+1.76}_{-1.6}$ | $31.21^{+5.25}_{-7.57}$ |
| 7084 | 137.025 | 1.331 | 0.66 | – | – | – |
| 885 | 137.308 | −0.204 | 0.31 | $2.99^{+0.52}_{-0.37}$ | $5.65^{+0.49}_{-0.44}$ | $14.52^{+1.38}_{-1.55}$ |
| 2004 | 137.314 | −1.018 | 0.82 | $5.57^{+4.09}_{-1.96}$ | $6.17^{+2.72}_{-3.36}$ | $21.12^{+10.09}_{-10.65}$ |
| 3523 | 137.386 | −0.839 | 1.13 | $5.61^{+2.19}_{-1.11}$ | $26.33^{+2.91}_{-3.09}$ | $93.83^{+11.49}_{-17.28}$ |
| 372 | 138.723 | 4.27 | 0.14 | $2.46^{+0.84}_{-0.67}$ | $1.8^{+0.11}_{-0.09}$ | $4.35^{+0.5}_{-0.4}$ |

**Table C2**  – *continued*

| eFEDS ID | RA | Dec. | $z$ | $T_{\rm x,500\,kpc}^{\rm XGA}$ | $L_{\rm x,500\,kpc}^{\rm XGA,52}$ | $L_{\rm x,500\,kpc}^{\rm XGA,bol}$ |
|---|---|---|---|---|---|---|
| 4253 | 138.801 | 4.585 | 0.36 | $5.18^{+-5.18}_{-3.76}$ | $1.18^{+0.3}_{-1.18}$ | $3.96^{+5.96}_{-1.84}$ |
| 534 | 139.042 | $-0.397$ | 0.32 | $6.04^{+0.35}_{-0.35}$ | $13.86^{+0.32}_{-0.34}$ | $49.42^{+1.96}_{-1.85}$ |
| 100 | 140.338 | 3.291 | 0.33 | $7.83^{+0.31}_{-0.31}$ | $19.66^{+0.25}_{-0.23}$ | $79.71^{+0.85}_{-1.93}$ |
| 857 | 140.55 | $-0.459$ | 0.32 | $5.86^{+0.24}_{-0.23}$ | $9.51^{+0.13}_{-0.11}$ | $33.41^{+0.66}_{-0.84}$ |
| 12565 | 142.473 | 0.467 | 0.15 | – | – | – |

*Notes.* $T_{\rm x,500\,kpc}^{\rm XGA}$ are temperatures within 500-kpc apertures, given in keV. $L_{\rm x,500\,kpc}^{\rm XGA,52}$ and $L_{\rm x,500\,kpc}^{\rm XGA,bol}$ are 0.5–2.0 keV and bolometric luminosities within a 500-kpc aperture, in units of $10^{43}{\rm erg\,s^{-1}}$. All uncertainties calculated from 68 per cent confidence limits, equivalent to $1\sigma$.

This paper has been typeset from a TEX/LATEX file prepared by the author.